Journal Pre-proofs

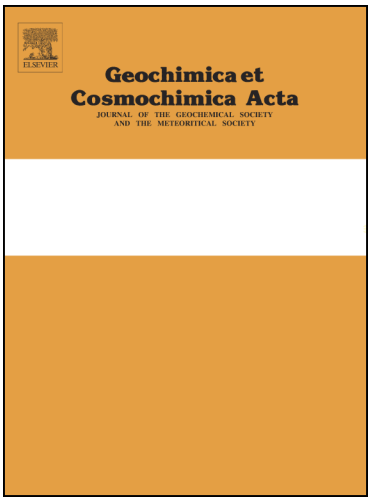

The chondritic neodymium stable isotope composition of the Earth inferred from mid-ocean ridge, ocean island and arc basalts

Alex J. McCoy-West, Kevin W. Burton, Marc-Alban Millet, Peter A. Cawood

PII: S0016-7037(20)30613-X
DOI: https://doi.org/10.1016/j.gca.2020.09.038
Reference: GCA 11945

To appear in: *Geochimica et Cosmochimica Acta*

Received Date: 13 May 2020
Revised Date: 29 September 2020
Accepted Date: 30 September 2020

Please cite this article as: McCoy-West, A.J., Burton, K.W., Millet, M-A., Cawood, P.A., The chondritic neodymium stable isotope composition of the Earth inferred from mid-ocean ridge, ocean island and arc basalts, *Geochimica et Cosmochimica Acta* (2020), doi: https://doi.org/10.1016/j.gca.2020.09.038

The chondritic neodymium stable isotope composition of the Earth inferred from mid-ocean ridge, ocean island and arc basalts

Alex J. McCoy-West[1,2,3], Kevin W. Burton[2], Marc-Alban Millet[4] and Peter. A. Cawood[1]

[1]*Department of Earth, Atmosphere and Environment, Monash University, Clayton, Victoria, 3800, Australia*

[2]*Department of Earth Sciences, Durham University, Elvet Hill, Durham DH1 3LE, UK*

[3]*Department of Earth and Environmental Sciences, James Cook University, Townsville, QLD 4811, Australia*

[4]*School of Earth and Ocean Sciences, Cardiff University, Park Place, Cardiff CF10 3AT, UK*

Number of words: 7,828

Number of references: 152

Number of figures: 12

Number of tables: 3

Corresponding author: Alex McCoy-West (alex.mccoywest@gmail.com)

Keywords: Nd isotopes; sulfide matte; magmatic differentiation; partial melting; mass-dependent fractionation; MORB; OIB; subduction zone.

ABSTRACT

Accurate knowledge of the composition of Earth's major chemical reservoirs is fundamental for constraining all modern geochemical cycles. Basaltic rocks provide a direct way of sampling the composition of Earth's inaccessible interior. Here, we present the first comprehensive neodymium (Nd) stable isotope analyses for a global compilation of mid-ocean ridge, ocean island, continental intraplate and island arc basalts using a double-spike technique. In these primitive magma compositions magmatic differentiation has no resolvable effect on $\delta^{146/144}$Nd. Mid-ocean ridge basalts possess an extremely homogenous $\delta^{146/144}$Nd with an average composition of $\delta^{146/144}$Nd = −0.025 ± 0.013 ‰ (± 2 s.d.; n = 33). Ocean island and continental intraplate magmas possess more variable compositions ($\delta^{146/144}$Nd = 62 ppm) that are related to the variable incorporation of recycled components in their source regions. Island arc basalts from New Britain ($\delta^{146/144}$Nd = 61 ppm) reflect the complex interplay between source composition, degree of melting and slab-fluid inputs. Variations are uncorrelated with indicators of magmatic differentiation or slab-fluid addition, rather increasing $\delta^{146/144}$Nd with slab depth is attributed to a higher proportion of metasomatized sub-arc mantle in the melting region. A partial melting model for Nd stable isotopes has been constructed using Nd−O force constants calculated using the Born-Lande approximation. Melting of typical mantle peridotite will induce no resolvable fractionations of Nd stable isotopes ($\Delta^{146/144}Nd_{melt\text{-}mantle}$ < 0.003 ‰ at 1200 °C). The lack of fractionation upon partial melting means primitive magmatic rocks can be used to calculate the average composition of the bulk silicate Earth (BSE), which is $\delta^{146/144}$Nd = −0.024 ± 0.031 ‰ (±2 s.d.; n = 80). This BSE composition is indistinguishable at the 95 % confidence level from that of chondritic meteorites, considered the building blocks of Earth. Therefore, sequestration of significant quantities of Nd into the sulfide matte did not occur, this combined with recent experimental evidence for no Sm-Nd fractionation means the sulfide matte cannot be considered a plausible solution for the ^{142}Nd/^{144}Nd offset between the Earth

and chondrites. Despite resolvable variations in $\delta^{146/144}$Nd from the canonical value being widespread in terrestrial materials, they are not large enough to generate the difference in radiogenic Nd isotope ratios between the BSE and chondrites.

1. INTRODUCTION

Basaltic rocks are the most voluminous and widespread magmas on Earth (Crisp, 1984), and provide an indirect means of sampling the composition of Earth's inaccessible interior. Therefore, they can be used to study the composition of the mantle, Earth's major silicate reservoir, and place constrains on the composition of the bulk silicate Earth (BSE; e.g. Sun and McDonough, 1989). Basaltic rocks have also been extensively used to trace the long-term recycling of surficial components into Earth's mantle (e.g. Elliott et al., 1999; Hofmann, 1997; Prytulak and Elliott, 2007; Sobolev et al., 2007; Stracke, 2012; Woodhead and Devey, 1993; Workman et al., 2004; Zindler and Hart, 1986) and the transfer of melt and fluids across the subduction interface into arc-basalts (e.g. Hildreth and Moorbath, 1988; Kent and Elliott, 2002; Spandler and Pirard, 2013; Woodhead et al., 1998). Over the last decade the application of novel stable isotopes to understand processes in the solid Earth has grown exponentially. At high temperatures, stable isotope fractionation can provide important insights into the conditions of magma genesis (Chen et al., 2013; Dauphas et al., 2009; Dauphas et al., 2014; Freymuth et al., 2015; Konter et al., 2016; McCoy-West et al., 2018; Nielsen et al., 2018; Nielsen et al., 2017; Sossi et al., 2012) or the processes involved in the formation and differentiation of planet Earth (Dauphas, 2017; Greber et al., 2017; McCoy-West et al., 2019; McCoy-West et al., 2017; Savage et al., 2015). However, stable isotope compositions are both source and process dependent with redox state and the local bonding environment controlling the composition of melts extracted from the mantle (e.g. Dauphas and Schauble, 2016; Schauble, 2004; Sossi and O'Neill, 2017; Young et al., 2015). At magmatic temperatures, the isotope fractionation induced during melting is generally minimal (Dauphas et al., 2009; McCoy-West et al., 2019; McCoy-West et al., 2018; Sossi et al., 2018), however, this fractionation needs to be accurately constrained prior to making inferences on the composition of the BSE.

Neodymium (Nd; Z = 60) is a refractory, lithophile (silicate-loving) element that has been widely utilised to understand the formation and evolution of the Earth. The long-lived ^{147}Sm-^{143}Nd decay system, where ^{147}Sm α decays to ^{143}Nd with a half-life of 106 Ga, has become an important chronometer and tracer that has been fundamental to advancing our understanding of planetary differentiation, crust formation and mantle heterogeneity on our planet (DePaolo, 1980; Jacobsen, 1988; Jacobsen and Wasserburg, 1984; McCulloch and Bennett, 1994). Radiogenic Nd isotopes are time-integrated tracers of source composition and therefore cannot directly place constraints on the processes and conditions under which these parent-daughter fractionations are occurring. Although, attempts to apply the complementary Nd stable isotope system, which can provide new insights on these processes using natural samples remain limited (McCoy-West et al., 2017, 2020a). This study presents high-precision double spike stable and radiogenic Nd isotope data for a global collection of mid-ocean ridge, ocean island, continental intraplate and island arc basalts. This dataset is used to discuss the process responsible for fractionating Nd stable isotopes, assess the causes of global mantle heterogeneity, and to trace fluid mobility in subduction zones. Finally, the composition of the BSE is defined and its implications for planetary differentiation are discussed.

2. SAMPLES

The samples investigated in this study are all well characterised (for major and trace elements ± radiogenic isotopes) and encompass all of the dominant types of basaltic magmatism on Earth including mid-ocean ridge basalts (MORB), ocean island basalts (OIB), continental intraplate basalts and subduction-related island arc basalts (IAB).

A global compilation of pristine MORB glasses (Fig. 1; Table 1) contains 14 samples from the Atlantic Ocean (Gannoun et al., 2007; Melson et al., 2002), including 12 samples from the plume-influenced FAMOUS segment of the Mid-Atlantic Ridge (Gale et al., 2013; Gannoun et al., 2004); and 13 samples from the Pacific Ocean (Gannoun et al., 2007; Schiano et al., 1997)

including 6 samples from the highly depleted Garret Fracture Zone region of the East Pacific Rise (Hékinian et al., 1995; Niu and Hékinian, 1997; Wendt et al., 1999). These new data are supplemented by six samples from across the Indian Ocean analysed previously (McCoy-West et al., 2020a).

Intraplate magmatism includes all magmas (basalts, picrites and komatiites) erupted away from plate boundaries that are unrelated to plate boundary processes. In this manuscript, for simplicity, intraplate magmatism is split into two major groups: OIB and other intraplate. OIB are partial melts that are probably derived from the deeper portions of the mantle (e.g. White, 2010), and possess a range of distinct mantle endmembers compositions in radiogenic isotope space reflecting the recycling of different components into their source regions (e.g. Hofmann, 2003; Stracke et al., 2005). In this study OIB from a wide geographic spread (Fig. 1) and with varied radiogenic isotope signatures (Fig. 2) were selected, including samples of EM-1 affinity from the Pitcairn Islands (n = 7; Devey et al., 2003; Hekinian et al., 2003), and high-μ (HIMU) magmas from the islands of Rurutu and Mangaia in the Cook-Austral Chain (Kogiso et al., 1997), and a sample with EM-2 affinity from Sao Miguel, in the Azores archipelago (Elliott et al., 2007). These samples are supplemented with previous analyses of OIB-type basaltic rock standards from Hawaii and Iceland (McCoy-West et al., 2017; McCoy-West et al., 2020b). The samples grouped as "other intraplate" comprise a diverse range of magmas that have been generated by significantly different melt fluxes from distinct origins. They include: 1) High-degree partial melts such as the primitive (high-MgO) 89 Ma Gorgona komatiites (Kerr, 2005; Kerr et al., 1996) and the 61 Ma Baffin Island picrites (McCoy-West et al., 2018; Starkey et al., 2009), which represent mantle melting at elevated temperatures (> 1400 °C), as well as Columbia River continental flood basalt, which underwent significant crustal assimilation (e.g. BCR; Brandon et al., 1993; Carlson et al., 1981); and 2) small melt fraction continental basalts, which are represented by the 98 Ma Lookout Volcanics, New Zealand

(McCoy-West et al., 2010) and possess a distinctive carbonatite related HIMU signature (Fig. 2; $^{206}Pb/^{204}Pb > 20.5$) that developed through rapid radiogenic ingrowth in the sub-continental lithospheric mantle (McCoy-West et al., 2016), and samples from the small volume monogenetic cones such as rock standard B-EN.

To provide the first constraints on subduction related magmatism modern IAB from New Britain, Papua New Guinea have been investigated (n = 12). These samples are derived from the Island Arc Basalt Reference Suite (Smithsonian Institution; BVSP, 1981) and have been previously characterized for their chemical and radiogenic isotope compositions (Woodhead et al., 1998; Woodhead and Johnson, 1993). The Quaternary volcanoes (< 1.8 Ma) of the New Britain arc formed through the northward subduction of the Solomon plate beneath the Bismarck plate. These samples record volcanism that extends over a large distance orthogonal to the subduction trench (ca. 100-300 km), and thus corresponds to a range of depths to the melting (Wadati–Benioff) zone from ≤ 100 km at the volcanic front to ~600 km beneath the Witu Islands (see Johnson, 1977).

3. METHODS

The analyses presented here were performed in the Arthur Holmes Geochemistry Labs at Durham University. Pristine basaltic glass from the interior of broken chips were hand-picked under a binocular microscope to obtain at least 20 mg per sample. To avoid artificially inducing stable isotope fractionations acid leaching of the glass was not undertaken. Glass and whole rock powders were then weighed (generally between 10-100 mg) to obtain 200 ng of natural Nd and then spiked with a $^{145}Nd-^{150}Nd$ double spike (60 % sample; 40 % spike). Samples were then dissolved using a conventional HF-HNO_3 (2:1) hotplate digestion at 120 °C for at least 48 hours. Multiple refluxes in concentrated HNO_3 and HCl were then undertaken to ensure the samples were completely dissolved. Neodymium was then separated using well-established chromatographic techniques (e.g. McCoy-West et al., 2016; Pin and Zalduegui, 1997). The rare

earth elements (REE) were separated from the sample matrix using BioRad AG50W-x8 cation exchange resin. Samples were loaded in 2 mL of 1M HCl, the matrix was then sequentially removed in 10 mL 1M HCl + 1M HF, 12 mL 2.5M HCl and 8 mL 2M HNO_3 with the REE fraction collected in 14 mL of 6M HCl. The REE fraction was then dried and Nd was separated from the other REE using elongated polypropylene columns filled with Eichrom Ln-Spec resin. Samples were loaded in 0.5 mL of 0.2M HCl, another 6 mL of 0.2M HCl was then eluted, prior to the collection of Nd in the next 6 mL of 0.2M HCl. This separation protocol results in nearly quantitative separation of Sm (isobaric interferences on ^{144}Nd, ^{148}Nd, and ^{150}Nd) from Nd (see Figure 3 in McCoy-West et al., 2020b). Total procedural blanks measured by isotope dilution were < 12 pg (n = 3) and in all cases, are negligible.

Neodymium isotope measurements were performed using a Thermo-Fisher *TritonPlus* thermal ionisation mass spectrometer (TIMS). In preparation for loading and TIMS analysis the solutions were evaporated to dryness and Nd samples individually loaded using 1 µL of 16M HNO_3 onto Re ionisation filaments in a double filament assembly. Neodymium was measured as a metallic ion in static collection mode using eight faraday cups (L4 = ^{142}Nd; L3 = ^{143}Nd; L2 = ^{144}Nd; L1 = ^{145}Nd; Ax = ^{146}Nd; H1 = ^{147}Sm; H2 = ^{148}Nd; H3 = ^{150}Nd). Samarium (^{147}Sm) was monitored and used to correct for isobaric interferences on ^{144}Nd, ^{148}Nd and ^{150}Nd. Each analysis usually comprised 400 cycles of data acquisition (8 sec per integration). Stable Nd isotope ratios are expressed using conventional delta notation, where $\delta^{146}Nd$, which is the per mil deviation in the measured $^{146}Nd/^{144}Nd$ relative to the widely measured reference standard JNdi-1:

$$\delta^{146/144}Nd = \left[\left(\frac{\frac{^{146}Nd}{^{144}Nd_{Sample}}}{\frac{^{146}Nd}{^{144}Nd_{JNdi-1}}}\right) - 1\right] \times 1000 \quad (1)$$

Double spike deconvolution was undertaken using the Wolfram Mathematica program and is based on the algebraic resolution method (Millet and Dauphas, 2014). As the radiogenic isotope

^{143}Nd is not used during double spike deconvolution, by projecting the measured composition to the mass fractionation line of JNdi-1 (see McCoy-West et al. (2020b) for equations), it is also possible to calculate the $^{143}Nd/^{144}Nd$ ratios from a single spiked aliquot. These values agree within analytical uncertainty of previously published values for conventional techniques (see Figure 1 in McCoy-West et al., 2017). The data presented here have been normalized so that $\delta^{146}Nd$ of JNdi-1 = 0 ‰, to correct for small offsets in the measured composition of JNdi-1 during different analytical periods due to differences in faraday collector efficiency (see Figure 3 in McCoy-West et al., 2020b). Propagated uncertainties were calculated using the 95 % standard error on the average of JNdi-1 for the correction period. Analytical uncertainties on a typical analysis are generally better than ± 0.006 ‰ and ± 5 ppm for $\delta^{146}Nd$ and $^{143}Nd/^{144}Nd$, respectively. To monitor instrument stability the JNdi-1 reference standard was measured on every analysis day and over a two-year period $^{143}Nd/^{144}Nd = 0.512108 \pm 19$ (n = 64; corrected for differences in faraday collector efficiency = 0.512112 ± 12) which is within uncertainty of previous estimates (Garçon et al., 2018; Rizo et al., 2011; Tanaka et al., 2000). Based on the replicate digestion (n = 5-8) of four USGS international rock standards (BHVO-1, BHVO-2, BIR-1 and G-2) over the same period the long-term reproducibility of the $\delta^{146}Nd$ measurements using the methodology herein is better than ± 0.015 ‰ (McCoy-West et al., 2017; McCoy-West et al., 2020b).

To provide an additional confirmation of the quality of the analyses herein the $\delta^{148}Nd$, which is the per mil deviation in $^{148}Nd/^{144}Nd$ relative to the reference standard JNdi-1 has also been calculated (Table 1). These $\delta^{148}Nd$ values are calculated following the double spike deconvolution calculations and are not forced to follow a mass dependent relationship. However, for the wide range of basaltic materials measured here the $\delta^{148}Nd$ values are generally ca. twice the $\delta^{146}Nd$ values, with most analyses falling close to the mass dependent fractionation line and within uncertainty of the long-term reproducibility of $\delta^{148}Nd$ (Fig. 3), thus confirming the accurate correction of mass bias induced by sample processing.

4. RESULTS

Mass-dependent and radiogenic Nd isotope compositions for the samples measured here are presented in Table 1. Although generally of a small magnitude, variations in δ^{146}Nd greater than analytical uncertainty occur in several basalt groups. Averages are provided to allow comparisons between the different basalt types.

4.1 Nd isotope variations in MORB

Stable Nd isotope compositions of MORB glasses display a restricted range from δ^{146}Nd = −0.045 ‰ to −0.009 ‰ (δ^{146}Nd = 36 ppm; Fig. 4). Neodymium concentrations range from 3.77 to 15.2 ppm and are broadly correlated with MgO content (Fig. 5a) but appear independent of location. Whereas radiogenic isotope compositions, although displaying a restricted range relative to the other magma types, with ε^{143}Nd from +7.7 to +12.9 (Fig. 4b) and $^{87}Sr/^{86}Sr$ from 0.7021 to 0.7032 (Fig. 5d), broadly delineate the distinct ocean basins consistent with previous observations (e.g. Hofmann, 2003). No correlation is observed between δ^{146}Nd and Nd concentration or ε^{143}Nd (Fig. 4), or indicators of magmatic differentiation (e.g. Mg# = molar $Mg/[Mg + Fe^{2+}]$; Fig. 5b) or mantle source enrichment (e.g. $La/Sm_{(N)}$; Fig. 5c). The average δ^{146}Nd composition of Atlantic MORB = −0.024 ± 0.015 ‰ (2 s.d.; n = 14; 95 % s.e. = ±0.004 ‰) and Pacific MORB = −0.025 ± 0.014 ‰ (2 s.d.; n = 13; 95 % s.e. = ±0.004 ‰) calculated here are identical within uncertainty to the previously reported δ^{146}Nd of Indian MORB = −0.026 ± 0.008 ‰ (n = 6; 95 % s.e. = ± 0.004 ‰; McCoy-West et al., 2020a). Due to the homogeneity of the MORB sample set, we can calculate a global average MORB composition of δ^{146}Nd = −0.025 ± 0.013 ‰ (n = 33; 95 % s.e. = ±0.002 ‰; Table 1; Fig. 6).

4.2 Nd isotope variations in OIB

Stable Nd isotope compositions of the majority of OIB show a minor range in δ^{146}Nd with values from −0.061 ‰ to −0.013 ‰ (δ^{146}Nd = 58 ppm; Fig. 4), with most samples being similar to, or slightly lighter than, average chondritic meteorites (Fig. 5; McCoy-West et al., 2017). Both the Nd concentration (14.8 to 83.0 ppm) and ε^{143}Nd (−3.8 to +6.7) are highly variable amongst the analysed OIB, however, no clear correlations are observed between δ^{146}Nd and either parameter (Fig. 4). These values exclude one anomalous Icelandic sample BIR-1 which possesses resolvably heavier δ^{146}Nd of 0.013 ± 0.015 ‰ (McCoy-West et al., 2020b), along with a very low Nd concentration of 2.33 ppm and more depleted MORB-like ε^{143}Nd composition (+8.8) due to its eruption in close proximity to the Mid-Atlantic Ridge (Fig. 1). Excluding the anomalous sample BIR-1, which also has a distinctive Ti isotope composition (Millet and Dauphas, 2014), the average δ^{146}Nd of OIB is calculated as −0.035 ± 0.026 ‰ (2 s.d.; n = 13; 95 % s.e. = ± 0.008 ‰; Fig. 6).

4.3 Nd isotope variations in other intraplate magmas

Measured stable Nd isotope compositions for the other intraplate magmas group are again variable with δ^{146}Nd ranging from −0.054 ‰ to 0.001 ‰ (δ^{146}Nd = 58 ppm; Fig. 6). Despite an extensive range in the MgO contents (3.5-29.2 wt %), Nd concentrations (1.79-66.4 ppm) and ε^{143}Nd (−0.1 to +11.1) of these magmas no correlations are observed with δ^{146}Nd (Fig. 4a-c). Although, magmas from different locations can possess resolvably different δ^{146}Nd, with the Lookout Volcanics all broadly chondritic with an average δ^{146}Nd of −0.022 ± 0.007 ‰ (n = 5; McCoy-West et al., 2020b), whereas the Gorgona komatiites are superchondritic with an average δ^{146}Nd of −0.004 ± 0.015 ‰ (n = 2; Fig. 6). Notwithstanding this small internal variability, the average δ^{146}Nd composition of the other intraplate magmas group is calculated as −0.026 ± 0.028 ‰ (n = 13; 95 % s.e. = ±0.008 ‰) which is identical within uncertainty to MORB and chondritic meteorites (Fig. 6).

4.4 Nd isotope variations in arc lavas

The New Britain IAB samples span the widest range of $\delta^{146}Nd$ observed from a single location with values ranging from −0.039 ‰ to 0.022 ‰ ($\delta^{146}Nd$ = 61 ppm; n = 12; Table 1). The IAB also have variable Nd concentrations from 1.68 to 24.9 ppm (Fig. 3a) but possess a rather uniform $\varepsilon^{143}Nd$ with values from 7.0 to 9.1 (average = 7.85 ± 1.15), excluding one sample (IA-2) that has resolvable lower $\varepsilon^{143}Nd$ of 5.3 (Fig. 3b). No correlations are observed between $\delta^{146}Nd$ and either SiO_2 (Fig. 7a) or MgO contents (Fig. 4c), for example, samples with a highly restricted range of SiO_2 from 51-53 wt % span the entire range of $\delta^{146}Nd$. Interestingly, correlations are observed between a range of large ion lithophile elements and $\delta^{146}Nd$, with moderate correlations observed with Ba and Rb ($r^2 > 0.5$; Fig. 7c-d). The average $\delta^{146}Nd$ composition of the New Britain IAB is −0.018 ± 0.033 ‰ (2 s.d.; n = 12; 95 % s.e. = ± 0.0011 ‰; Fig. 6) which is within uncertainty of the other magma types.

5. DISCUSSION

5.1 Causes of mass-dependent Nd isotope variability in primitive basalts

5.1.1. Alteration

Prior to interpreting the variations in $\delta^{146}Nd$ observed within the natural samples it is important to confirm they are related to magmatic processes. The magnitude of stable isotope fractionation in any isotope system is inversely proportional to temperature ($1/T^2$) and is proportional to the relative mass difference between the isotopes ($\Delta m/[m_1 + m_2]/2$) and a term derived from the difference in bonding environment between the phases of interest (Bigeleisen and Mayer, 1947; Schauble, 2004; Urey, 1947; Young et al., 2015). Surface weathering and alteration generally occurs at significant lower temperatures (< 50 °C) than

basaltic magma eruption (> 1000 °C), and therefore larger fractionations could be generated (i.e. proportional to $1/T^2$). However, Nd as a light (L)REE is extremely fluid immobile, and occurs in very low concentrations in low-temperature fluids (Nd < 40 ppt; Bau, 1991; Michard and Albarède, 1986) consequently, it is very robust to secondary modification. In this study, the freshest possible samples were selected to eliminate alteration as a factor in interpreting geochemical signals (i.e. hand-picking of optically pristine glasses or choosing well-characterised whole rock powders that could be screened for indicators of alteration). Notwithstanding this pre-selection, previous studies have shown that δ^{146}Nd is little affected by alteration (McCoy-West et al., 2017, 2020a). Analyses of samples that had experienced variable amounts of terrestrial alteration including a range of weakly altered gabbros from the oceanic crust (see Figure 9 in McCoy-West et al., 2020a) or chondritic meteorites which contain REE enriched sulfides that are extremely susceptible alteration (see Figure 6 in McCoy-West et al., 2017) show no systematic correlation between δ^{146}Nd and weathering intensity. Therefore, we are confident that the variations in δ^{146}Nd observed here are the result of magmatic processes.

5.1.2. Magmatic differentiation

Numerous studies have shown that magmatic differentiation can induce changes in the stable isotope composition of a magma (Chen et al., 2013; Inglis et al., 2019; McCoy-West et al., 2017; Millet et al., 2016; Savage et al., 2011; Schuessler et al., 2009; Sossi et al., 2012; Telus et al., 2012; Teng et al., 2008). At equilibrium for a specific element at a constant T, the magnitude of isotopic fractionation is controlled by the bonding term, which is dependent on the specific minerals crystallising and the differences between the redox state and bonding environment in the mineral and melt for the element of interest. Significant fractionations can be observed in the major structural constituents of silicate minerals (e.g. Si: Savage et al., 2011 up to 0.2 ‰) or oxide phases (e.g. Ti: Hoare et al., 2020 up to 2.3 ‰). However, for many

elements resolvable fractionations only occur at > 65 wt. % SiO_2 (Inglis et al., 2019; Schuessler et al., 2009; Telus et al., 2012), or for others no fractionation is observed at all (e.g. Zn: Chen et al., 2013; Mo: Yang et al., 2015). Although rare, in mafic magmas large fractionations can also occur due to diffusion-induced kinetic isotope exchange, as the result of elemental gradients (i.e. disequilibrium) between magmatic minerals and the coexisting melt (e.g. McCoy-West et al., 2019; McCoy-West et al., 2018; McCoy-West et al., 2020a; Sio et al., 2013; Weyer and Seitz, 2012).

The magnitude of isotopic fractionation is also controlled by proportion of the element that is transferred between the two phases under consideration (i.e. even if a large stable isotope fractionation does occur during a process, if transfer from one phase to the other is near quantitative there may be no measurable isotope fractionation). Neodymium is moderately to highly incompatible in most silicate phases and possesses only one valence state (Nd^{3+}), thus variations in $\delta^{146}Nd$ will be controlled by contrasts in the local bonding environment. Given Nd is a heavy element (Z = 60, $\Delta m/m$ for $^{146}Nd/^{144}Nd$ = 1.38 %) and is not a major structural constituent of any of the dominant mineral phases crystallising in basaltic magmas (e.g. olivine, clinopyroxene or plagioclase) it will preferentially remain in the melt, thus significant fractionation in $\delta^{146}Nd$ during magmatic differentiation is unlikely. Despite covering a wide range of SiO_2 contents, from 44-54 wt %, the mafic magmas studied here show limited variability in $\delta^{146}Nd$ and no resolvable correlation that could be related to magmatic differentiation (Fig. 4d). Looking specifically at MORB, no correlation is observed between $\delta^{146}Nd$ and Mg# a strong indicator of the degree of magmatic evolution (Fig. 5b). These results are consistent with previous analyses of a range of magmatic rock standards with < 70 wt % SiO_2 that display the same $\delta^{146}Nd$ within uncertainty over a wider range of SiO_2 contents (SiO_2 = 38-69 wt %; see Figure 5 in McCoy-West et al., 2017). The REE are very incompatible in olivine (D_{Nd} < 0.0002; Ionov et al., 2002; Sun and Liang, 2013) and therefore, despite being an

abundant phase in basaltic systems, from a mass balance perspective olivine hosts inconsequential amounts of Nd and can be excluded from consideration. Whereas the other major crystallising phases on the basaltic liquidus, clinopyroxene (D_{Nd} = 0.4-0.6; Hill et al., 2000) and plagioclase (D_{Nd} = 0.1-0.15; Bindeman and Davis, 2000) could conceivably host enough Nd to effect the δ^{146}Nd of an evolving melt. However, previous Rayleigh fractionation modelling (see Figure 10 in McCoy-West et al., 2020a) has shown that crystallising equal proportions of clinopyroxene and plagioclase (clinopyroxene dominants 80 % of the Nd budget) has no significant effect on δ^{146}Nd at geologically reasonable amounts of fractional crystallisation for a basalt (i.e. change in δ^{146}Nd is < 0.01‰ after 10 % crystallisation, which is within the long-term uncertainty of the measurements). This modelling was however based on a measured $\Delta^{146}Nd_{clinopyroxene\text{-}whole\ rock}$ from an ocean floor gabbro that had undergone kinetic isotope exchange and an estimated $\Delta^{146}Nd_{plagioclase\text{-}whole\ rock}$ value, therefore the true effects of fractional crystallisation under equilibrium conditions could be even smaller. Further work will be required to constrain possible fractionations of δ^{146}Nd in high SiO_2 magmas (> 65 wt %), but in primitive magmas ($SiO_2 \leq 54$ wt %) as studied here the effects of magmatic differentiation on δ^{146}Nd can be considered negligible.

5.1.3. Partial melting

Due to its high molar mass and the elevated temperatures of mantle melting, Nd stable isotope variations during melting would be predicted to be small. However, the large range of δ^{146}Nd in OIB (0.058 ‰; Fig. 6) relative to analytical precision (± 0.015 ‰), indicates that the effect of partial melting needs to be constrained. Neodymium behaves as an incompatible element during mantle melting ($D \leq 0.1$; Table 2), with simple peritectic melt modelling (McCoy-West et al., 2015) showing that > 80 % of the Nd budget, in both the spinel and garnet facies mantle, will be transferred to the extracted melt after only 10 % melting (see Figure A6 in McCoy-West

et al., 2017). Therefore, mass balance dictates that the original Nd stable isotope composition of the mantle source should be effectively recorded in melts. Evidence from the Garrett Fracture Zone supports this hypothesis with MORB glasses and their complementary abyssal peridotites showing no resolvable difference in δ^{146}Nd (McCoy-West et al., 2017). A further complication in constraining the effect of mantle melting is that it occurs at a range of depths, with the aluminous phase changing from spinel at intermediate pressure to garnet at higher pressures (Green and Ringwood, 1967). The REE are highly incompatible in spinel (DNd < 0.0006; Ionov et al., 2002), whereas in garnet the heavy REE are compatible and the middle REE moderately incompatible (D_{Yb} = 10.9 and D_{Sm} = 0.31, respectively, derived from Sun and Liang (2013) lattice strain model based on the garnet composition used herein from Walter (1998)). Therefore, trace element ratios such as $Sm/Yb_{(N)}$ can be used to trace the presence of the residual garnet in the source region of a melt (Hirschmann and Stolper, 1996; Humphreys and Niu, 2009). The varied range of magmas analysed here possess $Sm/Yb_{(N)}$ ratios from 0.66-7.3, which is consistent with melting over a wide depth range, however, no correlation is observed with δ^{146}Nd (Fig. 8).

Prior to constructing a model to constrain partial melting the force constants relevant for Nd ions in minerals and melts need to be determined. Here, to calculate force constants, we use the Born-Lande repulsion approximation (see Appendix A), which has been shown to be adequate for other condensed phases (Bourdon et al., 2018; McCoy-West et al., 2019; Sossi and O'Neill, 2017; Young et al., 2015). Using these force constants (Table 3) a non-modal batch melting model (Shaw, 1970) to show the fractionation of Nd stable isotopes during partial melting has then been constructed based upon the principles for isotopes outlined in Sossi and O'Neill (2017). Given that Nd is highly incompatible in spinel (DNd < 0.0006; Ionov et al., 2002) from a mass balance perspective, spinel will contribute insignificantly to the melting assemblage. Thus, the model developed here focuses on constraining melting in the garnet

stability field starting from a primitive mantle assemblage using experimental constrained peritectic melting proportions (see Table 2). A separate model needs to be constructed for each isotope of interest, with the partition coefficients for the heavier isotope adjusted, based on the calculated force constants for the minerals and melt and the temperature of melting:

$$D_{min-melt}^{^{146}\mathrm{Nd}} = \left(D_{min-melt}^{^{144}\mathrm{Nd}}\right)e^{\left(\frac{418.9\left(K_{Nd-O}^{min}-K_{Nd-O}^{melt}\right)}{T^2}\right)} \quad (2)$$

Where D refers to the partitioning coefficient of the different Nd isotopes, K is the total Nd force constants in the mineral and melt phase, T is temperature, and 418.9 is the constant value specific for Nd derived from the sum of vibrational frequencies (see Eq. A3). This model assumes melting under buffered, closed system conditions and therefore the composition of the minerals and hence K_{Nd-O}^{min}, is kept constant across all melt fractions. In combination, the two models can then be used to calculate $\Delta^{146}Nd_{melt\text{-}mantle}$ at various degrees of melting (Fig. 9). Clinopyroxene and garnet dominate the Nd budget of the melting assemblage (94.5 % and 5.5 %, respectively) consequently the bonding environment in the other phases is insignificant. Changing the mineral-melt partition coefficients has a minimal effect on the modelled Nd isotope composition of the melt, with changes to temperature or force constants being a far more sensitive parameters for driving larger isotopic fractionation (Fig. 9). Assuming that OIB are the result of at least 1 % melting at > 1200 °C $\Delta^{146}Nd_{melt\text{-}mantle}$ would only be ≤ 0.003 ‰, which is significantly smaller than the long-term reproducibility of δ^{146}Nd values (± 0.015 ‰). Therefore, this modelling demonstrates that typical mantle melting imparts no resolvable fractionation on δ^{146}Nd. However, this provides the possibility to use the Nd stable isotope composition of basaltic magmas as a source tracer or to constrain the composition of the BSE.

5.2 Using Nd stable isotope variability to trace components in the sources of primitive basalts

5.2.1. Tracing enriched mantle components?

It is well established from radiogenic isotopes that a range of long-lived heterogeneities exist in the mantle (Hofmann, 1997; Hofmann and White, 1982; Stracke et al., 2005; Zindler and Hart, 1986). Using stable isotope compositions, similar distinctions can be observed with the source regions of MORB (Andersen et al., 2015; Bezard et al., 2016; Nielsen et al., 2018), and OIB (Beunon et al., 2020; Konter et al., 2016; Williams and Bizimis, 2014), which are shown to contain a range of recycled components. Although, given that stable isotope compositions are process dependent, first the competing effects of magmatic differentiation and partial melting need to be removed to obtain the original isotopic composition of the melt prior to any interpretations being made. Fortunately for Nd (as discussed above) these effects are negligible. Therefore, Nd could be an ideal tracer of recycled components if they possess resolvably different δ^{146}Nd (which at this stage remains largely unknown). The global MORB dataset presented here spans the complete compositional range of MORB varying from normal-type (N-MORB: $La/Sm_{(N)} < 1.0$) to enriched-type (E-MORB: $La/Sm_{(N)} \geq 1.0$), with the latter shown to be the result of the incorporation of recycled sediments in the source region (Donnelly et al., 2004); however, no correlation is observed between $La/Sm_{(N)}$ and δ^{146}Nd (Fig. 5c). On the basis of Ba isotope mass balance modelling, Nielsen et al. (2018) showed that only ca. 0.1 % of recycled sedimentary material is required in the source regions of E-MORB, thus inducing an isotopic difference in E-MORB requires the addition of an exceedingly concentrated or isotopically fractionated component, which is probably not the case for Nd. The source regions of OIB are significantly more variable than MORB (Fig. 2) and have been explained by the recycling of variable amounts of oceanic crust ± sedimentary material with different compositions into their source regions (Rehkämper and Hofmann, 1997; Zindler and Hart,

1986). A significant range is observed in $\delta^{146}Nd$ for the OIB measured here ($\delta^{146}Nd$ = 58 ppm; Fig. 6), thus recycling may control this compositional variability. There is a hint within the OIB data that light $\delta^{146}Nd$ values are more common than for other magma types with an average value of −0.035‰ the lowest of any group. Previous analyses have shown that fragments of the oceanic crust have variable $\delta^{146}Nd$ compositions, with values as light as −0.13‰ generated by kinetic isotope exchange due to disequilibrium between percolating melts and the gabbro host rock (McCoy-West et al., 2020a), incorporation of this type of material into the source regions of OIB would be consistent with their lighter $\delta^{146}Nd$. For most elements, the addition of sediments has a significantly larger role on their final composition, with the sources of EM-type OIB having at least 5 % (but < 10 %) recycled sedimentary material (see Figure 8 in Stracke et al., 2003). Of the OIB samples herein the EM-1 type lavas from Pitcairn, contain the greatest proportion of recycled material and possess a significant range in both $\varepsilon^{143}Nd$ (0 to −4) and $\delta^{146}Nd$ (−0.055 to −0.013‰; Fig. 4b; Table 1). If the incorporation of recycled sedimentary components was the major driver of $\delta^{146}Nd$ variability a strong correlation with radiogenic isotopes would be expected. However, in the Pitcairn lavas only a weak correlation is observed between $\delta^{146}Nd$ and $\varepsilon^{143}Nd$ (r^2 = 0.32; excluding one sample; not shown). Given that Nd is only weakly enriched in pelagic sediments relative to basalts ($Nd_{sed}/Nd_{bas} \approx 2.4$; Stracke et al., 2003) compared to other incompatible elements (e.g. Based/Babas > 100; Nielsen et al., 2018), significantly larger amounts of sediment would be required to impart isotopic changes. Ultimately, to properly constrain the processes causing $\delta^{146}Nd$ variations in OIB, further work is required to constrain the composition of the recycled components (e.g. detrital and pelagic sediments) along with analysis of a broader suite of OIB.

5.2.2. Tracing variability across the mantle wedge?

Stable isotope systematics have also been increasingly utilised to understand the recycling of material at subduction zones and its transfer through the overlying mantle wedge to form arc basalts (e.g. Freymuth et al., 2015; Nielsen et al., 2017; Nielsen et al., 2020). Given that the New Britain IAB have the most variable $\delta^{146}Nd$ of the basalt-types investigated here further consideration is warranted. It is widely accepted that the trace element variability observed in arc lavas requires the mixing of, at least, three-components in their source region, namely sub-arc mantle peridotite, siliceous sedimentary melt and a slab-derived hydrous fluid component (Elliott et al., 1997; Hoogewerff et al., 1997). Woodhead et al. (1998) showed that the trace element variability within the New Britain arc is unrelated to magmatic differentiation (i.e. SiO_2 content) and instead suggested that chemical variation across the arc is controlled by the input of slab-derived fluids (see Figure 8 therein). Based on an expanded modern dataset, this simplified interpretation no longer holds for the broader arc, although the composition of the samples analysed herein is dominated by the addition of a slab-derived fluid component (Fig. 10a). The observed correlations between fluid mobile elements (e.g. Ba, Rb; see Fig. 7) and $\delta^{146}Nd$ suggests slab-derived fluids may be controlling this variability. However, when plotting $\delta^{146}Nd$ against trace element ratios commonly used to trace slab fluid mobility (i.e. Sr/Nd, Ba/Th and U/Nb; Fig. 10b-c) no correlations are observed with $\delta^{146}Nd$, meaning it is improbable that the addition of slab-derived fluids is controlling this variability.

The New Britain IAB studied here are erupted orthogonal to and at variable distances from the subduction trench (Fig. 11b) and therefore represent magmas generated over a wide range of melting depths (Holm and Richards, 2013; Johnson, 1977). Variations in their TiO_2 contents have previously been linked to a decrease in the amount of partial melting (and water content) with increasing depth (Woodhead et al., 1998; Woodhead and Johnson, 1993). This hypothesis is consistent with the negative correlations seen between TiO_2 and slab depth (Fig. 11a) and other incompatible elements (e.g. Th, Nb, Ce, not shown; i.e. the smallest melt

fractions from deeper regions are the most enriched in incompatible elements) and decreasing Ba/Th with depth (Fig. 11c; i.e. the melt zoning is more fluid rich at shallower depths). Dauphas et al. (2009) observed a positive correlation between $\delta^{56}Fe$ and TiO_2 content. For Nd, a similar weak positive correlation is observed between TiO_2 and $\delta^{146}Nd$ (Fig. 7b; excluding one sample), with a similarly weak correlation between $\delta^{146}Nd$ and slab depth (Fig. 11d). Given that fractionations induced by variable amounts of partial melting cannot generate resolvable variations in $\delta^{146}Nd$ (see Fig. 9), and the variability in $\delta^{146}Nd$ is uncorrelated with indicators of fluid addition (see Fig. 10), an additional mechanism is required. We attribute the marginally heavier $\delta^{146}Nd$ at greater depths to a higher proportion of metasomatized mantle in the melting region of these smaller volume partial melts. This heavy Nd signature could be imparted through the accumulation of small volume fractional melts in the source region or the liberation of a heavy Nd component into the mantle wedge during phase breakdown in down going slab. This data provides an intriguing hint that $\delta^{146}Nd$ may be tracing heterogeneity within the source region of arc lavas, but further work is required to investigate the causes of $\delta^{146}Nd$ variability in arc lavas more broadly as well as in mantle wedge peridotites.

5.3 The Nd stable isotope composition of the bulk silicate Earth

The first attempt to characterise the Nd stable isotope composition of BSE was based on a limited terrestrial database (n = 30; $\delta^{146}Nd = -0.022 \pm 0.034$ ‰ 2 s.d.; ± 0.006 ‰ 95 % s.e.; McCoy-West et al., 2017). This estimate only included 21 distinct samples and was biased by including multiple digestions of the same sample (e.g. BHVO-1; n = 5). Furthermore, it included a significant proportion of mantle samples (n = 8; > 25 %) which have highly variable $\delta^{146}Nd$ with values ranging from −0.045 ‰ to 0.029 ‰ (Fig. 12). Any heterogeneities induced during melting or secondary metasomatic events will be accentuated in these peridotites due to their significantly lower Nd concentrations (mostly <0.5 ppm; McCoy-West et al., 2020b) than basaltic melts. Consequently, here we present a revised estimate of the Nd stable isotope

composition of the BSE. As demonstrated above (see Section 5.1.3) partial melting has no resolvable effect on the δ^{146}Nd composition of basaltic melts (Fig. 9), therefore the measured values of primitive magmatic samples can be used to directly constrain the Nd stable isotope composition of the BSE. The MORB analysed here display a limited range and highly Gaussian distribution of δ^{146}Nd (Fig. 12b), consistent with being derived from an extremely homogenous reservoir. The other magmatic rocks, OIB, IAB and continental intraplate magmas all possess similar average compositions that are within uncertainty of the MORB (Fig 6). Therefore, it is reasonable to include all the measured samples presented here (plus the mantle samples) to calculate the revised average of composition of the BSE which is given as δ^{146}Nd = −0.024 ± 0.031 ‰ (2 s.d.; n = 80; ± 0.003 ‰ 95 % s.e.; Table 1).

5.4 Implications for planetary differentiation and the sulfide matte

Now that the δ^{146}Nd composition of the BSE is known we can explore its implications for the generation of ^{142}Nd/^{144}Nd anomalies. Pioneering TIMS analyses over a decade ago (Boyet and Carlson, 2005; Caro et al., 2003) showed that the Earth's mantle possesses a ^{142}Nd/^{144}Nd isotope composition that is ca. 20 ppm higher than chondritic meteorites, thought to be the building blocks of the terrestrial planets. Given that the parent radionuclide is now effectively extinct, with ^{146}Sm α-decaying to ^{142}Nd with a half-life of 103 Ma, the process that caused this fractionation must have occurred very soon after Solar System formation, while ^{146}Sm was still extant. This offset has been ascribed to a range of possibilities: 1) Earth's mantle experienced an early depletion event (< 30 Ma following accretion) resulting in the formation of an incompatible element enriched reservoir, the so-called hidden reservoir (Boyet and Carlson, 2005; Caro et al., 2003, 2006); 2) Earth's earliest silicate crust, which would complement the mantle, was removed through repeated large meteorite impacts during planetary construction, through so-called collisional erosion (O'Neill and Palme, 2008); 3) The formation of the sulfide

matte in the latter stages of core formation could act as an alternative hidden reservoir, due to the compatibility of the REE in sulfide under the highly reduced conditions of planetary formation (Wohlers and Wood, 2015); and, 4) The offset between the Earth and chondritic meteorites is instead a consequence of nucleosynthetic heterogeneities inherited from Solar nebula and no subsequent processing is necessary (Bouvier and Boyet, 2016; Boyet et al., 2018; Burkhardt et al., 2016).

Neodymium stable isotopes, unlike their radiogenic counterparts, provide a mechanism to test the validity of the sulfide matte solution. The late addition of volatile elements (e.g. S) and the removal of sulfide to the outer regions of the core (i.e. sulfide matte) during the final stages of accretion is predicted based on experimental work (Wade and Wood, 2005; Wade et al., 2012; Wood et al., 2014). Wohlers and Wood (2015) predicted, based on experiments at < 1650 °C, that core formation following the addition of a reduced sulfur-rich body to Earth could have generated a superchondritic Sm/Nd in the mantle and thus a suitable $^{142}Nd/^{144}Nd$ anomaly relative to chondrites. However, subsequent experimental work conducted at higher temperatures more analogous to core formation (> 2000 °C) challenges this idea with no significant fractionation between Sm and Nd observed (Bouhifd et al., 2015; Wohlers and Wood, 2017). For Nd, given it is monovalent, stable isotope partitioning is dominated by the local bonding environment. A significant contrast exists between the bond strength in sulfides and silicates, thus heavy isotopes should preferentially be incorporated into the high force-constant bonds involving REE^{3+} ions in silicate minerals, leaving a heavier residual mantle after the removal of a light isotope enriched sulfide phase This prediction is consistent with what has been observed for Cu, experimental results show light Cu isotopes preferentially partition into sulfide, and the BSE is resolvably heavier than chondritic meteorites which has been attributed to the removal of the sulfide matte (Savage et al., 2015). Following incorporation of all available data, the revised $\delta^{146}Nd$ composition of the BSE is −0.024 ± 0.003 ‰ (n = 80) which is

indistinguishable at the 95 % confidence level (Fig. 6) from the average composition of chondritic meteorites of −0.026 ± 0.004 ‰ (n = 40; McCoy-West et al., 2017). These two populations (Fig. 12) are also statistically indistinguishable using a students T-test (p-value > 0.45). The combination of evidence from Nd stable isotopes and recent experiments showing limited Sm-Nd fractionation at the conditions of core formation, means that the sulfide matte should no longer be consider a credible solution for the $^{142}Nd/^{144}Nd$ composition of the Earth. Collisional erosion implies substantial loss of Earth's heating producing elements (~50 %), which would have significantly change the cooling rate of the planet and is therefore also considered unlikely (Campbell and O'Neill, 2012). There is no conclusive geophysical evidence for a hidden silicate reservoir in the deep mantle, however, mantle convection over the last 4 Ga could easily have been mixed away this material. Given that $\delta^{146}Nd$ is unaffected by both remaining options currently debated within the community (nucleosynthetic effects and early silicate differentiation) we cannot eliminate either and therefore they both remain viable solutions for explaining the $^{142}Nd/^{144}Nd$ discrepancy.

5.5 The effect of variable $^{146}Nd/^{144}Nd$ on radiogenic Nd isotope measurements

Finally, we briefly explore the effects of variable $\delta^{146}Nd$ on conventional radiogenic Nd isotope measurements. Mass independent Nd isotope variations (i.e. both $^{143}Nd/^{144}Nd$ and $^{142}Nd/^{144}Nd$) in modern datasets are reported following normalisation to the assumed canonical stable isotope composition of $^{146}Nd/^{144}Nd = 0.7219$ (first used by O'Nions et al., 1977), which is equal to $\delta^{146}Nd = 0$ ‰. However, recent studies show that the assumption of constant $^{146}Nd/^{144}Nd$ does not hold (Herein; Ma et al., 2013; McCoy-West et al., 2017; McCoy-West et al., 2020a; McCoy-West et al., 2020b; Saji et al., 2016). This means the radiogenic Nd isotope values reported in the literature are not the "true" compositions of these materials. Although taking for example the −0.025 ‰ offset between the BSE and JNdi-1 the "true" $^{143}Nd/^{144}Nd$ and $^{142}Nd/^{144}Nd$ will be within analytical uncertainty of those conventional

reported. However, larger variations outside analytical uncertainty can be observed in the "true" $^{142}Nd/^{144}Nd$ (up to 10 ppm) in meteorites where variations in $\delta^{146}Nd$ are larger (range in $\delta^{146}Nd$ is 0.14 ‰; McCoy-West et al., 2017). Ultimately, the normalisation process cancels out this effect with the relative offset between samples maintained, furthermore the magnitude of fractionations in $\delta^{146}Nd$ are so small that no analytical artefacts for internally corrected isotope ratios (e.g. $^{142}Nd/^{144}Nd$) will be generated during this calculation. This is because the difference in slope between kinetic (i.e. lab induced) and equilibrium (i.e. natural processes) fractionation law for a high mass element like Nd over this fractionation range is minute and would not result in detectable anomalies.

6. CONCLUSIONS

High-precision double spike stable and radiogenic Nd isotope data for a global suite of mid-ocean ridge, ocean island, continental intraplate and island arc basalts have been used to provide following new insights into magma genesis:

1) A global collection of MORB glasses from the Atlantic, Indian and Pacific oceans possesses an extremely homogenous $\delta^{146}Nd$ with an average composition of $\delta^{146}Nd = -0.025 \pm 0.013$ ‰, consistent with a single process controlling the composition of this reservoir.
2) Ocean island and continental intraplate magmas possess more variable compositions ($\delta^{146}Nd$ from −0.061 ‰ to 0.013 ‰) that are probably the result of the variable incorporation of recycled components into their source regions. The lighter average composition of OIB ($\delta^{146}Nd = -0.035 \pm 0.026$ ‰) is consistent with this scenario, although further work is required to accurately constrain the composition of these components.
3) A theoretical partial melting model, developed based using Nd–O force constants calculated using a Born-Lande approximation, shows that no resolvable fractionations

of Nd stable isotopes will be generated upon partial melting of normal peridotite mantle ($\Delta^{146}Nd_{melt\text{-}mantle} \leq 0.003$ ‰ at 1200 °C).

4) The chemistry of the New Britain IAB is the result of a complex interplay between the degree of melting and slab-derived inputs both of which vary with depth. These samples show resolvable variations in $\delta^{146}Nd$ (−0.039 ‰ to 0.022 ‰) that are uncorrelated with indicators of magmatic differentiation or slab-fluid addition. Instead, variations in $\delta^{146}Nd$ with melting depth are attributed to a higher proportion of metasomatized sub-arc mantle in the melting region.
5) The average composition of the bulk silicate Earth ($\delta^{146}Nd = -0.024 \pm 0.003$ ‰) is indistinguishable at the 95 % confidence level from the building blocks of Earth chondritic meteorites ($\delta^{146}Nd = -0.026 \pm 0.004$ ‰). Therefore, sequestration of light Nd into the sulfide matte is improbable, combined with recent experimental evidence showing limited Sm-Nd fractionation at core forming conditions (e.g. Bouhifd et al., 2015), these results confirm that the sulfide matte can no longer be consider a credible solution for the $^{142}Nd/^{144}Nd$ offset between the Earth and chondrites.
6) Radiogenic Nd isotope analyses are conventionally reported relative to the canonical value of $^{146}Nd/^{144}Nd = 0.7219$, although there is now increasing evidence from $\delta^{146}Nd$ that this value is variable in natural materials. Luckily, the normalisation process cancels out this effect and given the small range of $\delta^{146}Nd$ values observed no artificial anomalies will be induced during this normalisation procedure.

Acknowledgements

Geoff Nowell and Chris Ottley are thanked for their laboratory maintenance and analytical support at Durham. Paolo Sossi is thanked for advice on implementation of the melting modelling. Tim Elliot, Godfrey Fitton and Andrew Kerr are thanked for generously providing intraplate samples. We are grateful to the Smithsonian Institution, Washington, for the loan of the island arc samples to AMW. This project was funded by the NERC grant NE/N003926/1 to KWB and ARC grant FL160100168 to PAC. We thank Andreas Stracke for editorial handling, and Michael Bizimis, Heye Freymuth and an anonymous reviewer for thoughtful reviews that helped make the manuscript stronger.

Research Data Statement

All research data associated with this manuscript is either provided in the Tables herein or the electronic supplementary annex.

APPENDIX A Application of the Born-Lande approximation to Nd isotopes

The following equations describe the Born-Lande repulsion approximation for the specific case of Nd, which was used here to calculate force constants that were utilised in the partial melting modelling. For simplicity, some intermediate equations have been omitted (see Sossi and O'Neill (2017) for a complete formulation). Changes in the bonding conditions of a cation can be generated by variations in the charge or coordination environment, which can be quantified by the bond valence principle (Pauling, 1929):

$$S = \frac{Z}{C_N} \quad \text{(A1)}$$

where S the average bond valence of a cation, is proportional to Z the average charge on the cation, and C_N the mean coordination number in the phase of interest. In the case of Nd, due to the single valence state (Nd^{3+}), variations are limited to changes in coordination environment. In silicate glass the coordination of the REE is highly composition dependent with VI-fold to IX-fold coordination observed (e.g. Ponader and Brown, 1989; Rao et al., 1983; Robinson, 1971). Sen and Stebbins (1995) showed extensive Nd_2O_3 clusters form in pure SiO_2 glass, however, the addition of Al_2O_3 (Al:Nd of 10:1) resulted in a homogeneous distribution of Nd ions in the glass due the relaxation of the Nd−O coordination polyhedral. Based on extended X-ray absorption fine structure (EXAFS) measurements, VI-fold coordination of Nd appears to dominate in silicate glasses (Sen, 2000). In minerals the coordination of a metal ion is controlled by the crystallographic site it enters. In clinopyroxene partitioning studies have shown the LREE are preferentially partitioned into the octahedrally (VIII-fold) coordinated M2 site (Bédard, 2014; Blundy et al., 1996; Cameron and Papike, 1981). In garnet (generic formula $X_3Al_2Si_3O_{12}$) partitioning studies and synchrotron measurements have shown that the REE replace the divalent X-site cations (mostly Ca^{2+}) in triangular dodecahedral (VIII-fold) coordination (Quartieri et al., 1999; Quartieri et al., 2002; Quartieri et al., 2004; Van Westrenen

et al., 1999; van Westrenen and Draper, 2007). Now considering isotopic fractionation, at equilibrium, the exchange of isotopes, *n* and *d* of an element, *E*, between two phases, *A* and *B*, is described by the fractionation factor, α:

$$\alpha^{\frac{n}{d}}E_{A-B} = \frac{\left(n_{E/d_E}\right)_A}{\left(n_{E/d_E}\right)_B} \quad \text{(A2)}$$

Under the harmonic approximation (Urey, 1947; which is reasonable given the high temperatures (>1000 K) under consideration here), the sum of all the vibrational frequencies in a phase can be written in terms of the force constant, *K* (Bigeleisen and Mayer, 1947; units N/m), yielding:

$$10^3 \ln \alpha^{\frac{n}{d}}E_{A-B} = \Delta^{\frac{n}{d}}E_{A-B} = \frac{10^3 3N_A}{96\pi^2}\left(\frac{h}{k_B T}\right)^2\left(\frac{1}{m_d}-\frac{1}{m_n}\right)[K_A - K_B] \quad \text{(A3)}$$

Where *h* is Planck's constant, k_B is Boltzmann's constant, *m* is the atomic mass of the isotope of interest, *T* is temperature in K. The $3N_A$ term (Avogadro's Number) comes from summation over all vibrations in condensed matter (Bigeleisen and Mayer, 1947). For a specific isotope ratio and element, most of the equation reduces to a constant value, in this case for Nd yielding:

$$\Delta^{\frac{146}{144}}Nd_{A-B} = 418.9\,\frac{[K_A - K_B]}{T^2} \quad \text{(A4)}$$

The force constant for the different phases, K_f, can then be approximated by solving the Born–Lande equation, after Young et al. (2009), which describes the elastic energy of an ionic lattice:

$$K_f^{Nd-O} = -\frac{_{NdO}q^2(1-B)}{4\pi\varepsilon_0 r^3} \quad \text{(A5)}$$

where *q* is the charge on an electron, *B* is the Born exponent (which is dependent on lattice compressibility and taken to be 12 for minerals; Young et al., 2009), ε_0 is Coulomb's constant and *r* is the bond length in metres. Here, we have used measured Nd–O bond lengths (Clark et al., 1969; Quartieri et al., 2002; Sen, 2000) to calculate the force constants using this equation, and they are given in Table A1. The accuracy of the measured bond lengths in the minerals have been confirmed using the Shannon Radius approximation (Shannon, 1976). Where the

mean Nd–O bond distance is the sum of the Shannon ionic radius for the Nd species ($^{VI}Nd^{3+}$ = 98.3 pm; $^{VIII}Nd^{3+}$ = 110.9 pm) in the appropriate co-ordination environment and that of O^{2-} (138 pm). Bond stiffness, as quantified by K_f above, is estimated assuming solely electrostatic interactions between the metal cation and the relevant oxygen anions. However, this treatment does not consider differences in bonding environment of ions with different electronegativities, $\mathcal{X}$. Therefore, to calculate the total force constant, the ionicity, *I*, of the cation of interest needs to be calculated using the empirical expression of Pauling (1932):

$$I = 1 - e^{-\frac{1}{4}(\mathcal{X}_{Nd} - \mathcal{X}_O)^2} \quad \text{(A6)}$$

Recognition that ionic bonds contribute only 3/4 of the total bond strength in this case, for Nd−O bonds the ionicity is 0.733, allows a scaling factor to be applied to derive the total force constant, K_T:

$$K_T^{Nd-O} = \frac{1}{4}\frac{K_f^{Nd-O} C_N}{I} \quad \text{(A7)}$$

Values of K_T are presented in Table A1 and range from 2.0 to 2.7 times larger than K_f, depending on the coordination number. The total Nd force constants calculated here are significantly smaller than those obtained in previous studies for transition metals (McCoy-West et al., 2019; Sossi and O'Neill, 2017). This is a function of: 1) the significantly longer Nd bond length (as the force constant is proportional to $1/r^3$; Eq (A5)); 2) the slightly higher ionicity (as the force constant is proportional to $1/I$; Eq (A7)); and, 3) the smaller relative mass difference between ^{146}Nd and ^{144}Nd (hence the small value of the constant in Eq (A3)).

Figure Captions:

Figure 1: Map showing the global distribution of the various types of magmatic samples discussed in this study. Base map and bathymetry is from Ryan et al. (2009).

Figure 2: (a) Sr-Nd and (b) Sr-Pb isotope plots comparing the mafic magmas studied here and the major mantle end-member compositions. Samples are plotted using the $\varepsilon^{143}Nd$ measured herein. Literature data sources are as follows: MORB: Schiano et al. (1997), Gale et al. (2013) and Wendt et al. (1999); OIB: Elliott et al. (2007) and Kogiso et al. (1997); Other intraplate: McCoy-West et al. (2010), Starkey et al. (2009) and Jochum et al. (2016); New Britain IAB: Woodhead and Johnson (1993). Mantle endmember fields are based on the data presented in Hofmann (2014). The Lookout Volcanics data have been age-corrected for radiogenic ingrowth. The samples measured here from Pitcairn Island have no published Pb values and their compositions have been inferred from the Sr-Nd isotope data, using previously published isotope data from Pitcairn (Woodhead and McCulloch, 1989; Woodhead and Devey, 1993) which shows excellent correlations in Sr-Nd-Pb space (small open circles: $r^2 > 0.93$), to demonstrate their EM-1 affinity.

Figure 3: Plot showing the mass dependent covariation between $\delta^{146}Nd$ and $\delta^{148}Nd$ for samples measured in this study. Most analyses fall within uncertainty of the equilibrium mass-dependent fractionation line (EMFL; Slope = 2.00037). Hollow symbols represent individual analyses of the basaltic rock standards measured previously (McCoy-West et al., 2017; McCoy-West et al., 2020b). The shaded field represents an uncertainty in $\delta^{148}Nd$ of ± 0.038 ‰, which is based on the long-term uncertainty in $\delta^{146}Nd$ (± 0.015 ‰) but has been increased proportionally based on the relative mass difference between the isotopes and the less precise counting statistics due to the smaller ion beam on ^{148}Nd.

Figure 4: Variations in the $\delta^{146}Nd$ of magmatic rocks formed in a variety of tectonic settings. Graphs of $\delta^{146}Nd$ versus Nd concentration (a), $\varepsilon^{143}Nd$ (b) using the measurements herein, and $\delta^{146}Nd$ versus published MgO (c) and SiO_2 (d) contents. Error bars on $\delta^{146}Nd$ are propagated 2 standard errors. Data is sourced from herein (n = 55) but also published sources (n = 25; McCoy-West et al., 2017, 2020a; McCoy-West et al., 2020b). Major element data is compiled from references cited in Figure 2.

Figure 5: Variability of mid-ocean ridge basalts with samples distinguished based on ocean basin. (a) Nd concentration versus MgO content. Comparative global MORB data (circles) come from Jenner and O'Neill (2012). Variation in $\delta^{146}Nd$ relative to Mg# (b) and $La/Sm_{(N)}$ (c) and $^{87}Sr/^{86}Sr$ (d), respectively. Values are chondrite normalized using Palme and O'Neill (2014). Normal-type MORB (N-MORB: $La/Sm_{(N)} < 1.0$) and enriched-type MORB (E-MORB: $La/Sm_{(N)} \geq 1.0$) are distinguished in (c). The shaded area shows ± 2 standard deviations from the MORB average (−0.025 ± 0.016 ‰), with the dotted lines representing the 95% standard error of the mean (± 0.003 ‰).

Figure 6: Comparison of the $\delta^{146}Nd$ in a range of terrestrial magmatic rocks. Error bars on most of the data points are propagated 2 standard errors, whereas the rock standards are plotted with the long-term reproducibility (± 0.015 ‰) given they are averages of multiply digestions. The light grey shaded area represents the chondritic average ± 2 standard deviations (−0.026 ± 0.025 ‰; McCoy-West et al., 2017) with the dark grey band representing the 95% standard error of the mean (± 0.004 ‰). The shaded areas for the different groups show ± 2 standard deviations from the mean, with the dotted lines representing the 95% standard error of the mean (see Table 1 for further information).

Figure 7: Whole rock variations of $\delta^{146}Nd$ in New Britain island arc basalts versus the SiO_2 (a) and TiO_2 (b) contents, and Ba (c) and Rb (d) concentrations. All samples are plotted with long term errors on $\delta^{146}Nd$ (±0.015‰). Error ellipses are calculated using Isoplot (Ludwig, 2008) using the long-term uncertainty on $\delta^{146}Nd$ and assuming a 5% uncertainty on the trace element data. Major and trace element data is derived from BVSP (1981).

Figure 8: Plot of $\delta^{146}Nd$ versus $Sm/Yb_{(N)}$. Values are chondrite normalized using Palme and O'Neill (2014). Data sources are the same as Figure 2. Incompatible trace element ratios are unaffected by fractional crystallization and therefore can be used as tracers of source mineralogy. Values of $Sm/Yb_{(N)} > 1$ are consistent with residual garnet in the source region of a magma (see text for discussion).

Figure 9: Partial melting model showing the degree of enrichment of heavy Nd isotopes in a melts generated by melting of typical mantle peridotite at a range of temperatures between 1000 °C and 1400 °C. Two batch melting models are shown which vary due to changing the

force constants for Nd−O bonds in the melt (i.e. $C_O = 4$ or $C_O = 3$ in the melt; see Table 3 for further details). The dotted lines represent models of fractional melting and accumulated fractional melting at 1200 °C assuming the C_O (i.e. coordination of oxygen) in the melt is 4.

Figure 10: (a) Plot of Th/Yb versus Sr/Nd shown to assess the sources contributing arc lavas after Woodhead et al. (1998). The New Britain IAB samples analysed here are compared to published datasets from the broader New Britain (fluid-dominated; e.g. Woodhead and Johnson, 1993) and Lesser Antilles (sediment-dominated; e.g. Carpentier et al., 2008) arcs using data download from www.georoc.org. Datasets were filtered to only include volcanic rocks with a loss on ignition of < 2 wt % and SiO_2 contents of < 57 wt %. The distribution of the data suggests that the process resulting in the enrichment of Sr are distinct from those which enrich Th (see text for further discussion). (b-c) Variations of $\delta^{146}Nd$ in New Britain IAB versus trace element ratios indicative of slab fluid addition, Sr/Nd (b) and Ba/Th (c).

Figure 11: (a) Plot of TiO_2 content verses slab depth. The depth to the New Britain slab for each sample was calculated based on the distance from the trench and the depth of the Wadati-Benioff zone as presented in Johnson (1977), which agrees well with the model of Holm and Richards (2013). A ± 50 km error bar has been added to the depth estimates. (b) Map showing the location of the New Britain IAB with respect to the subduction trench. Base map and bathymetry is from Ryan et al. (2009), this is overlaid with a model showing the depth to the subducting slab from Holm and Richards (2013). (c-d) Graphs of slab depth versus Ba/Th (c) and $\delta^{146}Nd$ (d).

Figure 12: Histograms of $\delta^{146}Nd$ comparing the compositional distribution of some major magmatic reservoirs (a) chondritic meteorites (McCoy-West et al., 2017), enstatite chondrites are distinguished in dark blue (b) mid-ocean ridge basalts (c) the bulk silicate Earth, mantle peridotites are plotted in green. Terrestrial data is compilation of new samples measured herein (n = 55) and previously published data (n = 25; McCoy-West et al., 2017, 2020a; McCoy-West et al., 2020b). Lines overlying the histogram represent relative probability density plots.

Table Captions

Table 1: Uncertainties on measured $^{143}Nd/^{144}Nd$ and $\delta^{146}Nd$ and $\delta^{148}Nd$ are 2 standard errors. To represent population uncertainty, both the two standard deviation (2 s.d.) and 95% standard errors (95% s.e. = t * s.d./(n)1/2, where t = inverse survival function of the Student's t-test at the 95% significance level and (n-1) degrees of freedom) are presented for averages. $\varepsilon^{143}Nd$ is calculated based on measured compositions, with $\varepsilon^{143}Nd = [(^{143}Nd/^{144}Nd_{Sample}/^{143}Nd/^{144}Nd_{CHUR}) -1] \times 10{,}000$; where $^{143}Nd/^{144}Nd_{CHUR} = 0.512638$ (Jacobsen and Wasserburg, 1984). () Numbers in parentheses represent a duplicate digestion. * represents a duplicate analysis on a different filament. ^ OIB average excludes rock standard BIR-1. $ Data has been previously published (McCoy-West et al., 2017, 2020a; McCoy-West et al., 2020b) and is included for comparison. $\delta^{146}Nd_{NORM}$ values are measured $\delta^{146}Nd$ values that have been normalised to JNdi-1 = 0‰ and uncertainties have been propagated. All $^{143}Nd/^{144}Nd$ values have been corrected to $^{143}Nd/^{144}Nd$ in JNdi-1 = 0.512112 (Rizo et al., 2011).

Table 2: *Melting parameters assuming melting at 3 GPa come from Walter (1998). ^ Partition coefficients are calculated using the mineral compositions in Walter (1998; Run 30.05) and derived using compositional and temperature dependent lattice strain models (Sun and Liang, 2012, 2013; Yao et al., 2012) assuming a temperature of 1200 °C. Modelling uses the force constants calculated in Table 3.

Table 3: C_N = coordination number. $\bar{S}$ = the average bond valence. $r_{Nd-O}M$ = measured Nd−O bond length in pm (1 x 10^{-12} m). Measured Nd−O bond lengths are from 1) Sen (2000); 2) Clark et al. (1969); 3) Quartieri et al. (2004). $r_{Nd-O}Cal$ = calculated Nd−O bond length are based on the approximation that the mean Nd−O bond distance is the sum of the Shannon ionic radius for the Nd species in the appropriate coordination environment and that of O^{2-}. K_f^{Nd-O} = is the force constant approximated by solving the Born-Landé equation. K_T^{Nd-O} = is the total force constant corrected by a scaling factor related to the proportion of ionic bonds (the ionicity of the Nd−O bond based on the Pauling scale is 0.733; Pauling, 1932). In silicate melts O bonded to Nd will be either III- or IV-fold coordinated (Sen, 2000), here we have modelled both scenarios (see Fig. 9) to encompass the full range. In clinopyroxene there are 3 types of O, 2 that IV-fold coordinated and one that is III-fold coordinated (around the M2 site where Nd will be located there a 4 O3 oxygens (IV-fold), 2 O3 oxygens (III-fold) and 2 O1

oxygens (IV-fold); Cameron and Papike, 1981) with an average C_N of 3.75. Due to the rigid crystal lattice of garnet only IV-fold coordinated O is observed (Novak and Gibbs, 1971). Orthopyroxene and olivine host negligible Nd and are not substantial involved in the melting assemblage (see Table 2) thus for simplicity their force constants (K_T) have been assumed to be the same as clinopyroxene.

REFERENCES

Andersen, M.B., Elliott, T., Freymuth, H., Sims, K.W.W., Niu, Y. and Kelley, K.A. (2015) The terrestrial uranium isotope cycle. Nature 517, 356.
Bau, M. (1991) Rare-earth element mobility during hydrothermal and metamorphic fluid-rock interaction and the significance of the oxidation state of europium. Chemical Geology 93, 219-230.
Bédard, J.H. (2014) Parameterizations of calcic clinopyroxene—Melt trace element partition coefficients. Geochemistry, Geophysics, Geosystems 15, 303-336.
Beunon, H., Mattielli, N., Doucet, L.S., Moine, B. and Debret, B. (2020) Mantle heterogeneity through Zn systematics in oceanic basalts: Evidence for a deep carbon cycling. Earth-Science Reviews, 103174.
Bezard, R., Fischer-Gödde, M., Hamelin, C., Brennecka, G.A. and Kleine, T. (2016) The effects of magmatic processes and crustal recycling on the molybdenum stable isotopic composition of Mid-Ocean Ridge Basalts. Earth and Planetary Science Letters 453, 171-181.
Bigeleisen, J. and Mayer, M.G. (1947) Calculation of Equilibrium Constants for Isotopic Exchange Reactions. The Journal of Chemical Physics 15, 261-267.
Bindeman, I.N. and Davis, A.M. (2000) Trace element partitioning between plagioclase and melt: investigation of dopant influence on partition behavior. Geochimica et Cosmochimica Acta 64, 2863-2878.
Blundy, J.D., Wood, B.J. and Davies, A. (1996) Thermodynamics of rare earth element partitioning between clinopyroxene and melt in the system CaO-MgO-Al_2O_3-SiO_2. Geochimica et Cosmochimica Acta 60, 359-364.
Bouhifd, M.A., Boyet, M., Cartier, C., Hammouda, T., Bolfan-Casanova, N., Devidal, J.L. and Andrault, D. (2015) Superchondritic Sm/Nd ratio of the Earth: Impact of Earth's core formation. Earth and Planetary Science Letters 413, 158-166.
Bourdon, B., Roskosz, M. and Hin, R.C. (2018) Isotope tracers of core formation. Earth-Science Reviews 181, 61-81.
Bouvier, A. and Boyet, M. (2016) Primitive Solar System materials and Earth share a common initial 142Nd abundance. Nature 537, 399-402.
Boyet, M., Bouvier, A., Frossard, P., Hammouda, T., Garçon, M. and Gannoun, A. (2018) Enstatite chondrites EL3 as building blocks for the Earth: The debate over the 146Sm–142Nd systematics. Earth and Planetary Science Letters 488, 68-78.
Boyet, M. and Carlson, R.W. (2005) 142Nd evidence for early (>4.53 Ga) global differentiation of the silicate Earth. Science 309, 576-581.
Brandon, A.D., Hooper, P.R., Goles, G.G. and Lambert, R.S.J. (1993) Evaluating crustal contamination in continental basalts: the isotopic composition of the Picture Gorge Basalt of the Columbia River Basalt Group. Contributions to Mineralogy and Petrology 114, 452-464.
Burkhardt, C., Borg, L.E., Brennecka, G.A., Shollenberger, Q.R., Dauphas, N. and Kleine, T. (2016) A nucleosynthetic origin for the Earth's anomalous 142Nd composition. Nature 537, 394-398.
BVSP, B.V.S.P. (1981) Island Arc Basalts, Basaltic Volcanism on the Terrestrial Planets. Pergamon Press, Inc., New York, pp. pg. 193-213.
Cameron, M. and Papike, J.J. (1981) Structural and chemical variations in pyroxenes. American Mineralogist 66, 1-50.
Campbell, I.H. and O'Neill, H.S.C. (2012) Evidence against a chondritic Earth. Nature 483, 553-558.
Carlson, R.W., Lugmair, G.W. and Macdougall, J.D. (1981) Columbia River volcanism: the question of mantle heterogeneity or crustal contamination. Geochimica et Cosmochimica Acta 45, 2483-2499.
Caro, G., Bourdon, B., Birck, J.-L. and Moorbath, S. (2003) ^{146}Sm–^{142}Nd evidence from Isua metamorphosed sediments for early differentiation of the Earth's mantle. Nature 423, 428.
Caro, G., Bourdon, B., Birck, J.-L. and Moorbath, S. (2006) High-precision 142Nd/144Nd measurements in terrestrial rocks: Constraints on the early differentiation of the Earth's mantle. Geochimica et Cosmochimica Acta 70, 164-191.
Carpentier, M., Chauvel, C. and Mattielli, N. (2008) Pb–Nd isotopic constraints on sedimentary input into the Lesser Antilles arc system. Earth and Planetary Science Letters 272, 199-211.

Chen, H., Savage, P.S., Teng, F.-Z., Helz, R.T. and Moynier, F. (2013) Zinc isotope fractionation during magmatic differentiation and the isotopic composition of the bulk Earth. Earth and Planetary Science Letters 369, 34-42.
Clark, J.R., Appleman, D.E. and Papike, J.J. (1969) Crystal-chemical characterization of clinopyroxenes based on eight new structure refinements. Mineralogical Society Of America Special Paper 2, 31-50.
Crisp, J.A. (1984) Rates of magma emplacement and volcanic output. Journal of Volcanology and Geothermal Research 20, 177-211.
Dauphas, N. (2017) The isotopic nature of the Earth's accreting material through time. Nature 541, 521.
Dauphas, N., Craddock, P.R., Asimow, P.D., Bennett, V.C., Nutman, A.P. and Ohnenstetter, D. (2009) Iron isotopes may reveal the redox conditions of mantle melting from Archean to Present. Earth and Planetary Science Letters 288, 255-267.
Dauphas, N., Roskosz, M., Alp, E.E., Neuville, D.R., Hu, M.Y., Sio, C.K., Tissot, F.L.H., Zhao, J., Tissandier, L., Médard, E. and Cordier, C. (2014) Magma redox and structural controls on iron isotope variations in Earth's mantle and crust. Earth and Planetary Science Letters 398, 127-140.
Dauphas, N. and Schauble, E.A. (2016) Mass Fractionation Laws, Mass-Independent Effects, and Isotopic Anomalies. Annual Review of Earth and Planetary Sciences 44, 709-783.
DePaolo, D.J. (1980) Crustal growth and mantle evolution: inferences from models of element transport and Nd and Sr isotopes. Geochimica et Cosmochimica Acta 44, 1185-1196.
Devey, C.W., Lackschewitz, K.S., Mertz, D.F., Bourdon, B., Cheminée, J.-L., Dubois, J., Guivel, C., Hékinian, R. and Stoffers, P. (2003) Giving birth to hotspot volcanoes: Distribution and composition of young seamounts from the seafloor near Tahiti and Pitcairn islands. Geology 31, 395-398.
Donnelly, K.E., Goldstein, S.L., Langmuir, C.H. and Spiegelman, M. (2004) Origin of enriched ocean ridge basalts and implications for mantle dynamics. Earth and Planetary Science Letters 226, 347-366.
Elliott, T., Blichert-Toft, J., Heumann, A., Koetsier, G. and Forjaz, V. (2007) The origin of enriched mantle beneath São Miguel, Azores. Geochimica et Cosmochimica Acta 71, 219-240.
Elliott, T., Plank, T., Zindler, A., White, W. and Bourdon, B. (1997) Element transport from slab to volcanic front at the Mariana arc. Journal of Geophysical Research: Solid Earth 102, 14991-15019.
Elliott, T., Zindler, A. and Bourdon, B. (1999) Exploring the kappa conundrum: The role of recycling in the lead isotope evolution of the mantle. Earth and Planetary Science Letters 169, 129-145.
Freymuth, H., Vils, F., Willbold, M., Taylor, R.N. and Elliott, T. (2015) Molybdenum mobility and isotopic fractionation during subduction at the Mariana arc. Earth and Planetary Science Letters 432, 176-186.
Gale, A., Laubier, M., Escrig, S. and Langmuir, C.H. (2013) Constraints on melting processes and plume-ridge interaction from comprehensive study of the FAMOUS and North Famous segments, Mid-Atlantic Ridge. Earth and Planetary Science Letters 365, 209-220.
Gannoun, A., Burton, K.W., Parkinson, I.J., Alard, O., Schiano, P. and Thomas, L.E. (2007) The scale and origin of the osmium isotope variations in mid-ocean ridge basalts. Earth and Planetary Science Letters 259, 541-556.
Gannoun, A., Burton, K.W., Thomas, L.E., Parkinson, I.J., van Calsteren, P. and Schiano, P. (2004) Osmium isotope heterogeneity in the constituent phases of mid-ocean ridge basalts. Science 303, 70-72.
Garçon, M., Boyet, M., Carlson, R.W., Horan, M.F., Auclair, D. and Mock, T.D. (2018) Factors influencing the precision and accuracy of Nd isotope measurements by thermal ionization mass spectrometry. Chemical Geology 476, 493-514.
Greber, N.D., Dauphas, N., Bekker, A., Ptáček, M.P., Bindeman, I.N. and Hofmann, A. (2017) Titanium isotopic evidence for felsic crust and plate tectonics 3.5 billion years ago. Science 357, 1271-1274.
Green, D.H. and Ringwood, A.E. (1967) The stability fields of aluminous pyroxene peridotite and garnet peridotite and their relevance in upper mantle structure. Earth and Planetary Science Letters 3, 151-160.
Hékinian, R., Bideau, D., Hébert, R. and Niu, Y. (1995) Magmatism in the Garrett transform fault (East Pacific Rise near 13°27′S). Journal of Geophysical Research: Solid Earth 100, 10163-10185.

Hekinian, R., Cheminée, J.L., Dubois, J., Stoffers, P., Scott, S., Guivel, C., Garbe-Schönberg, D., Devey, C., Bourdon, B., Lackschewitz, K., McMurtry, G. and Le Drezen, E. (2003) The Pitcairn hotspot in the South Pacific: distribution and composition of submarine volcanic sequences. Journal of Volcanology and Geothermal Research 121, 219-245.
Hildreth, W. and Moorbath, S. (1988) Crustal contributions to arc magmatism in the Andes of Central Chile. Contributions to Mineralogy and Petrology 98, 455-489.
Hill, E., Wood, B.J. and Blundy, J.D. (2000) The effect of Ca-Tschermaks component on trace element partitioning between clinopyroxene and silicate melt. Lithos 53, 203-215.
Hirschmann, M.M. and Stolper, E.M. (1996) A possible role for garnet pyroxenite in the origin of the "garnet signature" in MORB. Contributions to Mineralogy and Petrology 124, 185-208.
Hoare, L., Klaver, M., Saji, N.S., Gillies, J., Parkinson, I.J., Lissenberg, C.J. and Millet, M.-A. (2020) Melt chemistry and redox conditions control titanium isotope fractionation during magmatic differentiation. Geochimica et Cosmochimica Acta 282, 38-54.
Hofmann, A.W. (1997) Mantle geochemistry: the message from oceanic volcanism. Nature 385, 219.
Hofmann, A.W. (2003) Sampling mantle heterogeneity through oceanic basalts: Isotopes and trace elements, Treatise of Geochemistry. Elsevier Ltd., pp. 61-101.
Hofmann, A.W. (2014) 3.3 - Sampling Mantle Heterogeneity through Oceanic Basalts: Isotopes and Trace Elements, in: Holland, H.D., Turekian, K.K. (Eds.), Treatise on Geochemistry (Second Edition). Elsevier, Oxford, pp. 67-101.
Hofmann, A.W. and White, W.M. (1982) Mantle plumes from ancient oceanic crust. Earth and Planetary Science Letters 57, 421-436.
Holm, R.J. and Richards, S.W. (2013) A re-evaluation of arc–continent collision and along-arc variation in the Bismarck Sea region, Papua New Guinea. Aust. J. Earth Sci. 60, 605-619.
Hoogewerff, J.A., Van Bergen, M.J., Vroon, P.Z., Hertogen, J., Wordel, R., Sneyers, A., Nasution, A., Varekamp, J.C., Moens, H.L.E. and Mouchel, D. (1997) U-series, Sr□Nd□Pb isotope and trace-element systematics across an active island arc-continent collision zone: Implications for element transfer at the slab-wedge interface. Geochimica et Cosmochimica Acta 61, 1057-1072.
Humphreys, E.R. and Niu, Y. (2009) On the composition of ocean island basalts (OIB): The effects of lithospheric thickness variation and mantle metasomatism. Lithos 112, 118-136.
Inglis, E.C., Moynier, F., Creech, J., Deng, Z., Day, J.M.D., Teng, F.-Z., Bizzarro, M., Jackson, M. and Savage, P. (2019) Isotopic fractionation of zirconium during magmatic differentiation and the stable isotope composition of the silicate Earth. Geochimica et Cosmochimica Acta 250, 311-323.
Ionov, D.A., Bodinier, J.-L., Mukasa, S.B. and Zanetti, A. (2002) Mechanisms and sources of mantle metasomatism: Major and trace element compositions of peridotite xenoliths from Spitsbergen in the context of numerical modelling. Journal of Petrology 43, 2219-2259.
Jacobsen, S.B. (1988) Isotopic and chemical constraints on mantle-crust evolution. Geochimica et Cosmochimica Acta 52, 1341-1350.
Jacobsen, S.B. and Wasserburg, G.J. (1984) Sm-Nd isotopic evolution of chondrites and achondrites, II. Earth and Planetary Science Letters 67, 137-150.
Jenner, F.E. and O'Neill, H.S.C. (2012) Major and trace analysis of basaltic glasses by laser-ablation ICP-MS. Geochemistry, Geophysics, Geosystems 13, Q03003.
Jochum, K.P., Weis, U., Schwager, B., Stoll, B., Wilson, S.A., Haug, G.H., Andreae, M.O. and Enzweiler, J. (2016) Reference Values Following ISO Guidelines for Frequently Requested Rock Reference Materials. Geostandards and Geoanalytical Research 40, 333-350.
Johnson, R.W. (1977) Distribution and major element chemistry of late Cainozoic volcanoes at the southern margin of the Bismarck Sea, Papua New Guinea. Australian Bureau of Mineral Resources Report, Canberra, Australia, p. p. 188.
Kent, A.J.R. and Elliott, T.R. (2002) Melt inclusions from Marianas arc lavas: implications for the composition and formation of island arc magmas. Chemical Geology 183, 263-286.
Kerr, A.C. (2005) La Isla de Gorgona, Colombia: A petrological enigma? Lithos 84, 77-101.
Kerr, A.C., Marriner, G.F., Arndt, N.T., Tarney, J., Nivia, A., Saunders, A.D. and Duncan, R.A. (1996) The petrogenesis of Gorgona komatiites, picrites and basalts: new field, petrographic and geochemical constraints. Lithos 37, 245-260.

Kogiso, T., Tatsumi, Y., Shimoda, G. and Barsczus, H.G. (1997) High μ (HIMU) ocean island basalts in southern Polynesia: New evidence for whole mantle scale recycling of subducted oceanic crust. Journal of Geophysical Research: Solid Earth 102, 8085-8103.
Konter, J.G., Pietruszka, A.J., Hanan, B.B., Finlayson, V.A., Craddock, P.R., Jackson, M.G. and Dauphas, N. (2016) Unusual δ56Fe values in Samoan rejuvenated lavas generated in the mantle. Earth and Planetary Science Letters 450, 221-232.
Ludwig, K.R. (2008) Isoplot 3.71, 3.71 ed. Berkeley Geochronology Centre.
Ma, J., Wei, G., Liu, Y., Ren, Z., Xu, Y. and Yang, Y. (2013) Precise measurement of stable neodymium isotopes of geological materials by using MC-ICP-MS. Journal of Analytical Atomic Spectrometry 28, 1926-1931.
McCoy-West, A.J., Baker, J.A., Faure, K. and Wysoczanski, R. (2010) Petrogenesis and origins of mid-Cretaceous continental intraplate volcanism in Marlborough, New Zealand: Implications for the long-lived HIMU magmatic mega-province of the SW Pacific. Journal of Petrology 51, 2003-2045.
McCoy-West, A.J., Bennett, V.C. and Amelin, Y. (2016) Rapid Cenozoic ingrowth of isotopic signatures simulating "HIMU" in ancient lithospheric mantle: Distinguishing source from process. Geochimica et Cosmochimica Acta 187, 79-101.
McCoy-West, A.J., Bennett, V.C., O'Neill, H.S.C., Hermann, J. and Puchtel, I.S. (2015) The interplay between melting, refertilization and carbonatite metasomatism in off-cratonic lithospheric mantle under Zealandia: An integrated major, trace and platinum group element study. Journal of Petrology 56, 563-604.
McCoy-West, A.J., Chowdhury, P., Burton, K.W., Sossi, P., Nowell, G.M., Fitton, J.G., Kerr, A.C., Cawood, P.A. and Williams, H.M. (2019) Extensive crustal extraction in Earth's early history inferred from molybdenum isotopes. Nature Geoscience 12, 946-951.
McCoy-West, A.J., Godfrey Fitton, J., Pons, M.-L., Inglis, E.C. and Williams, H.M. (2018) The Fe and Zn isotope composition of deep mantle source regions: Insights from Baffin Island picrites. Geochimica et Cosmochimica Acta 238, 542-562.
McCoy-West, A.J., Millet, M.-A. and Burton, K.W. (2017) The neodymium stable isotope composition of the silicate Earth and chondrites. Earth and Planetary Science Letters 480, 121-132.
McCoy-West, A.J., Millet, M.-A. and Burton, K.W. (2020a) The neodymium stable isotope composition of the oceanic crust: Reconciling the mismatch between erupted mid-ocean ridge basalts and lower crustal gabbros. Frontiers in Earth Science 8.
McCoy-West, A.J., Millet, M.-A., Nowell, G.M., Nebel, O. and Burton, K.W. (2020b) Simultaneous measurement of neodymium stable and radiogenic isotopes from a single aliquot using a double spike. Journal of Analytical Atomic Spectrometry 35, 388-402.
McCulloch, M.T. and Bennett, V.C. (1994) Progressive growth of the Earth's continental crust and depleted mantle: Geochemical constraints. Geochimica et Cosmochimica Acta 58, 4717-4738.
Melson, W.G., O'Hearn, T. and Jarosewich, E. (2002) A data brief on the Smithsonian Abyssal Volcanic Glass Data File. Geochemistry, Geophysics, Geosystems 3, 1-11.
Michard, A. and Albarède, F. (1986) The REE content of some hydrothermal fluids. Chemical Geology 55, 51-60.
Millet, M.-A. and Dauphas, N. (2014) Ultra-precise titanium stable isotope measurements by double-spike high resolution MC-ICP-MS. Journal of Analytical Atomic Spectrometry 29, 1444-1458.
Millet, M.-A., Dauphas, N., Greber, N.D., Burton, K.W., Dale, C.W., Debret, B., Macpherson, C.G., Nowell, G.M. and Williams, H.M. (2016) Titanium stable isotope investigation of magmatic processes on the Earth and Moon. Earth and Planetary Science Letters 449, 197-205.
Nielsen, S.G., Horner, T.J., Pryer, H.V., Blusztajn, J., Shu, Y., Kurz, M.D. and Le Roux, V. (2018) Barium isotope evidence for pervasive sediment recycling in the upper mantle. Science Advances 4.
Nielsen, S.G., Prytulak, J., Blusztajn, J., Shu, Y., Auro, M., Regelous, M. and Walker, J. (2017) Thallium isotopes as tracers of recycled materials in subduction zones: Review and new data for lavas from Tonga-Kermadec and Central America. Journal of Volcanology and Geothermal Research 339, 23-40.
Nielsen, S.G., Shu, Y., Auro, M., Yogodzinski, G., Shinjo, R., Plank, T., Kay, S.M. and Horner, T.J. (2020) Barium isotope systematics of subduction zones. Geochimica et Cosmochimica Acta 275, 1-18.

Niu, Y. and Hékinian, R. (1997) Basaltic liquids and harzburgitic residues in the Garrett Transform: A case study at fast-spreading ridges. Earth and Planetary Science Letters 146, 243-258.
Novak, G.A. and Gibbs, G.V. (1971) The crystal chemistry of the silicate garnets. American Mineralogist 56, 791-825.
O'Neill, H.S.C. and Palme, H. (2008) Collisional erosion and the non-chondritic composition of the terrestrial planets. Philosophical Transactions of the Royal Society A: Mathematical, Physical and Engineering Sciences 366, 4205-4238.
O'Nions, R.K., Hamilton, P.J. and Evensen, N.M. (1977) Variations in143Nd/144Nd and87Sr/86Sr ratios in oceanic basalts. Earth and Planetary Science Letters 34, 13-22.
Palme, H. and O'Neill, H.S.C. (2014) Cosmochemical estimates of mantle composition. Treatise on Geochemistry 2.1.
Pauling, L. (1929) The principles determining the structure of complex ionic crystals. Journal of the American Chemical Society 51, 1010-1026.
Pauling, L. (1932) The nature of the chemical bond IV. The energy of single bonds and the relative electronegativity of atoms. Journal of the American Chemical Society 54, 3570-3582.
Pin, C. and Zalduegui, J.S. (1997) Sequential separation of light rare-earth elements, thorium and uranium by miniaturized extraction chromatography: Application to isotopic analyses of silicate rocks. Analytica Chimica Acta 339, 79-89.
Ponader, C.W. and Brown, G.E. (1989) Rare earth elements in silicate glassmelt systems: I. Effects of composition on the coordination environments of La, Gd, and Yb. Geochimica et Cosmochimica Acta 53, 2893-2903.
Prytulak, J. and Elliott, T. (2007) TiO2 enrichment in ocean island basalts. Earth and Planetary Science Letters 263, 388-403.
Quartieri, S., Antonioli, G., Geiger, C.A., Artioli, G. and Lottici, P.P. (1999) XAFS characterization of the structural site of Yb in synthetic pyrope and grossular garnets. Physics and Chemistry of Minerals 26, 251-256.
Quartieri, S., Boscherini, F., Chaboy, J., Dalconi, M.C., Oberti, R. and Zanetti, A. (2002) Characterization of trace Nd and Ce site preference and coordination in natural melanites: a combined X-ray diffraction and high-energy XAFS study. Physics and Chemistry of Minerals 29, 495-502.
Quartieri, S., Dalconi, M.C., Boscherini, F., Oberti, R. and D'Acapito, F. (2004) Changes in the local coordination of trace rare-earth elements in garnets by high-energy XAFS: new data on dysprosium. Physics and Chemistry of Minerals 31, 162-167.
Rao, K.J., Wong, J. and Weber, M.J. (1983) Bonding and structure of Nd3+ in BeF2 glass by XANES and EXAFS spectroscopy. The Journal of Chemical Physics 78, 6228-6237.
Rehkämper, M. and Hofmann, A.W. (1997) Recycled ocean crust and sediment in Indian Ocean MORB. Earth and Planetary Science Letters 147, 93-106.
Rizo, H., Boyet, M., Blichert-Toft, J. and Rosing, M. (2011) Combined Nd and Hf isotope evidence for deep-seated source of Isua lavas. Earth and Planetary Science Letters 312, 267-279.
Robinson, C.C. (1971) Evidence of Sixfold Coordination of Nd3+ in Barium Rubidium Silicate Glass. The Journal of Chemical Physics 54, 3572-3578.
Ryan, W.B.F., Carbotte, S.M., Coplan, J.O., O'Hara, S., Melkonian, A., Arko, R., Weissel, R.A., Ferrini, V., Goodwillie, A., Nitsche, F., Bonczkowski, J. and Zemsky, R. (2009) Global multi-Resolution topography synthesis. Geochemistry, Geophysics, Geosystems 10, Q03014.
Saji, N.S., Wielandt, D., Paton, C. and Bizzarro, M. (2016) Ultra-high-precision Nd-isotope measurements of geological materials by MC-ICPMS. Journal of Analytical Atomic Spectrometry 31, 1490-1504.
Savage, P.S., Georg, R.B., Williams, H.M., Burton, K.W. and Halliday, A.N. (2011) Silicon isotope fractionation during magmatic differentiation. Geochimica et Cosmochimica Acta 75, 6124-6139.
Savage, P.S., Moynier, F., Chen, H., Shofner, G., Siebert, J., Badro, J. and Puchtel, I.S. (2015) Copper isotope evidence for large-scale sulphide fractionation during Earth's differentiation. Geochemical Perspectives Letters 1, 53-64.
Schauble, E.A. (2004) Applying Stable Isotope Fractionation Theory to New Systems. Reviews in Mineralogy and Geochemistry 55, 65-111.

Schiano, P., Birck, J.-L. and Allègre, C.J. (1997) Osmium-strontium-neodymium-lead isotopic covariations in mid-ocean ridge basalt glasses and the heterogeneity of the upper mantle. Earth and Planetary Science Letters 150, 363-379.
Schuessler, J.A., Schoenberg, R. and Sigmarsson, O. (2009) Iron and lithium isotope systematics of the Hekla volcano, Iceland — Evidence for Fe isotope fractionation during magma differentiation. Chemical Geology 258, 78-91.
Sen, S. (2000) Atomic environment of high-field strength Nd and Al cations as dopants and major components in silicate glasses: a Nd LIII-edge and Al K-edge X-ray absorption spectroscopic study. Journal of Non-Crystalline Solids 261, 226-236.
Sen, S. and Stebbins, J.F. (1995) Structural role of Nd3+ and Al3+ cations in SiO2 glass: a 29Si MAS-NMR spin-lattice relaxation, 27Al NMR and EPR study. Journal of Non-Crystalline Solids 188, 54-62.
Shannon, R. (1976) Revised effective ionic radii and systematic studies of interatomic distances in halides and chalcogenides. Acta Crystallographica Section A 32, 751-767.
Shaw, D.M. (1970) Trace element fractionation during anatexis. Geochimica et Cosmochimica Acta 34, 237-243.
Sio, C.K.I., Dauphas, N., Teng, F.-Z., Chaussidon, M., Helz, R.T. and Roskosz, M. (2013) Discerning crystal growth from diffusion profiles in zoned olivine by in situ Mg–Fe isotopic analyses. Geochimica et Cosmochimica Acta 123, 302-321.
Sobolev, A.V., Hofmann, A.W., Kuzmin, D.V., Yaxley, G.M., Arndt, N.T., Chung, S.L., Danyushevsky, L.V., Elliott, T., Frey, F.A., Garcia, M.O., Gurenko, A.A., Kamenetsky, V.S., Kerr, A.C., Krivolutskaya, N.A., Matvienkov, V.V., Nikogosian, I.K., Rocholl, A., Sigurdsson, I.A., Sushchevskaya, N.M. and Teklay, M. (2007) The amount of recycled crust in sources of mantle-derived melts. Science 316, 412-417.
Sossi, P.A., Foden, J.D. and Halverson, G.P. (2012) Redox-controlled iron isotope fractionation during magmatic differentiation: an example from the Red Hill intrusion, S. Tasmania. Contributions to Mineralogy and Petrology 164, 757-772.
Sossi, P.A., Nebel, O., O'Neill, H.S.C. and Moynier, F. (2018) Zinc isotope composition of the Earth and its behaviour during planetary accretion. Chemical Geology 477, 73-84.
Sossi, P.A. and O'Neill, H.S.C. (2017) The effect of bonding environment on iron isotope fractionation between minerals at high temperature. Geochimica et Cosmochimica Acta 196, 121-143.
Spandler, C. and Pirard, C. (2013) Element recycling from subducting slabs to arc crust: A review. Lithos 170-171, 208-223.
Starkey, N.A., Stuart, F.M., Ellam, R.M., Fitton, J.G., Basu, S. and Larsen, L.M. (2009) Helium isotopes in early Iceland plume picrites: Constraints on the composition of high 3He/4He mantle. Earth and Planetary Science Letters 277, 91-100.
Stracke, A. (2012) Earth's heterogeneous mantle: A product of convection-driven interaction between crust and mantle. Chemical Geology 330-331, 274-299.
Stracke, A., Bizimis, M. and Salters, V.J.M. (2003) Recycling oceanic crust: Quantitative constraints. Geochemistry, Geophysics, Geosystems 4, 8003.
Stracke, A., Hofmann, A.W. and Hart, S.R. (2005) FOZO, HIMU, and the rest of the mantle zoo. Geochemistry Geophysics Geosystems 6.
Sun, C. and Liang, Y. (2012) Distribution of REE between clinopyroxene and basaltic melt along a mantle adiabat: Effects of major element composition, water, and temperature. Contributions to Mineralogy and Petrology 163, 807-823.
Sun, C. and Liang, Y. (2013) The importance of crystal chemistry on REE partitioning between mantle minerals (garnet, clinopyroxene, orthopyroxene, and olivine) and basaltic melts. Chemical Geology 358, 23-36.
Sun, S.S. and McDonough, W.F. (1989) Chemical and isotopic systematics of oceanic basalts: implications for mantle composition and processes, in: Saunders, A.D., Norry, M.J. (Eds.), Magmatism in ocean basins. Geological Society of London special publication, pp. 313-345.
Tanaka, T., Togashi, S., Kamioka, H., Amakawa, H., Kagami, H., Hamamoto, T., Yuhara, M., Orihashi, Y., Yoneda, S., Shimizu, H., Kunimaru, T., Takahashi, K., Yanagi, T., Nakano, T., Fujimaki, H., Shinjo, R., Asahara, Y., Tanimizu, M. and Dragusanu, C. (2000) JNdi-1: a neodymium isotopic reference in consistency with LaJolla neodymium. Chemical Geology 168, 279-281.

Telus, M., Dauphas, N., Moynier, F., Tissot, F.L.H., Teng, F.-Z., Nabelek, P.I., Craddock, P.R. and Groat, L.A. (2012) Iron, zinc, magnesium and uranium isotopic fractionation during continental crust differentiation: The tale from migmatites, granitoids, and pegmatites. Geochimica et Cosmochimica Acta 97, 247-265.
Teng, F.-Z., Dauphas, N. and Helz, R.T. (2008) Iron Isotope Fractionation During Magmatic Differentiation in Kilauea Iki Lava Lake. Science 320, 1620-1622.
Urey, H.C. (1947) The thermodynamic properties of isotopic substances. Journal of the Chemical Society (Resumed), 562-581.
Van Westrenen, W., Blundy, J. and Wood, B.J. (1999) Crystal-chemical controls on trace element partitioning between garnet and anhydrous silicate melt. American Mineralogist 84, 838-847.
van Westrenen, W. and Draper, D.S. (2007) Quantifying garnet-melt trace element partitioning using lattice-strain theory: new crystal-chemical and thermodynamic constraints. Contributions to Mineralogy and Petrology 154, 717-730.
Wade, J. and Wood, B.J. (2005) Core formation and the oxidation state of the Earth. Earth and Planetary Science Letters 236, 78-95.
Wade, J., Wood, B.J. and Tuff, J. (2012) Metal–silicate partitioning of Mo and W at high pressures and temperatures: Evidence for late accretion of sulphur to the Earth. Geochimica et Cosmochimica Acta 85, 58-74.
Walter, M.J. (1998) Melting of garnet peridotite and the origin of komatiite and depleted lithosphere. Journal of Petrology 39, 29-60.
Wendt, J.I., Regelous, M., Niu, Y., Hékinian, R. and Collerson, K.D. (1999) Geochemistry of lavas from the Garrett Transform Fault: insights into mantle heterogeneity beneath the eastern Pacific. Earth and Planetary Science Letters 173, 271-284.
Weyer, S. and Seitz, H.M. (2012) Coupled lithium- and iron isotope fractionation during magmatic differentiation. Chemical Geology 294-295, 42-50.
White, W.M. (2010) Oceanic Island Basalts and Mantle Plumes: The Geochemical Perspective. Annual Review of Earth and Planetary Sciences 38, 133-160.
Williams, H.M. and Bizimis, M. (2014) Iron isotope tracing of mantle heterogeneity within the source regions of oceanic basalts. Earth and Planetary Science Letters 404, 396-407.
Wohlers, A. and Wood, B.J. (2015) A Mercury-like component of early Earth yields uranium in the core and high mantle 142Nd. Nature 520, 337-340.
Wohlers, A. and Wood, B.J. (2017) Uranium, thorium and REE partitioning into sulfide liquids: Implications for reduced S-rich bodies. Geochimica et Cosmochimica Acta 205, 226-244.
Wood, B.J., Kiseeva, E.S. and Mirolo, F.J. (2014) Accretion and core formation: The effects of sulfur on metal–silicate partition coefficients. Geochimica et Cosmochimica Acta 145, 248-267.
Woodhead, J. and McCulloch, M. (1989) Ancient seafloor signals in Pitcairn Island lavas and evidence for large amplitude, small length-scale mantle heterogeneities. Earth and Planetary Science Letters 94, 257-273.
Woodhead, J.D. and Devey, C.W. (1993) Geochemistry of the Pitcairn seamounts, I: source character and temporal trends. Earth and Planetary Science Letters 116, 81-99.
Woodhead, J.D., Eggins, S.M. and Johnson, R.W. (1998) Magma Genesis in the New Britain Island Arc: Further Insights into Melting and Mass Transfer Processes. Journal of Petrology 39, 1641-1668.
Woodhead, J.D. and Johnson, R.W. (1993) Isotopic and trace-element profiles across the New Britain island arc, Papua New Guinea. Contributions to Mineralogy and Petrology 113, 479-491.
Workman, R.K., Hart, S.R., Jackson-Matthew, G., Regelous, M., Farley, K.A., Blusztajn, J., Kurz, M.D. and Staudigel, H. (2004) Recycled metasomatized lithosphere as the origin of the enriched mantle II (EM2) end-member: Evidence from the Samoan volcanic chain. Geochemistry Geophysics Geosystems 5, Q04008, doi:04010.01029/02003GC000623.
Yang, J., Siebert, C., Barling, J., Savage, P., Liang, Y.-H. and Halliday, A.N. (2015) Absence of molybdenum isotope fractionation during magmatic differentiation at Hekla volcano, Iceland. Geochimica et Cosmochimica Acta 162, 126-136.
Yao, L., Sun, C. and Liang, Y. (2012) A parameterized model for REE distribution between low-Ca pyroxene and basaltic melts with applications to REE partitioning in low-Ca pyroxene along a mantle

adiabat and during pyroxenite-derived melt and peridotite interaction. Contributions to Mineralogy and Petrology 164, 261-280.
Young, E.D., Manning, C.E., Schauble, E.A., Shahar, A., Macris, C.A., Lazar, C. and Jordan, M. (2015) High-temperature equilibrium isotope fractionation of non-traditional stable isotopes: Experiments, theory, and applications. Chemical Geology 395, 176-195.
Young, E.D., Tonui, E., Manning, C.E., Schauble, E. and Macris, C.A. (2009) Spinel–olivine magnesium isotope thermometry in the mantle and implications for the Mg isotopic composition of Earth. Earth and Planetary Science Letters 288, 524-533.
Zindler, A. and Hart, S.R. (1986) Chemical geodynamics. Annual Reviews of Earth and Planetary Science 14, 493-571.

Table 1: Neodymium concentrations, radiogenic and mass dependent isotopic compositions of terrestrial basalts.

Sample	Type	Location	MgO (wt %)	Nd (ppm)	$^{143}Nd/^{144}Nd$	$\varepsilon^{143}Nd$	$\delta^{146/144}Nd$	$\delta^{148/144}Nd$	$\delta^{146/144}Nd_{NORM}$	2 s.d.	*n*
Mid-Ocean Ridge											
Atlantic Ocean											
"45N"	glass		9.01	9.17	0.513066 ±4	8.36	-0.007 ±0.007	-0.013 ±0.016	-0.026 ±0.007		
ALV518-3-2	glass	FAMOUS	7.68	8.37	0.513120 ±3	9.41	-0.006 ±0.005	-0.047 ±0.013	-0.025 ±0.006		
ALV519-2-1	glass	FAMOUS	9.41	4.75	0.513102 ±3	9.05	-0.001 ±0.004	-0.032 ±0.010	-0.020 ±0.005		
ALV519-2-3	glass	FAMOUS	9.35	4.74	0.513093 ±3	8.89	-0.008 ±0.005	-0.029 ±0.012	-0.027 ±0.006		
ALV522-1-1	glass	FAMOUS	9.61	4.87	0.513100 ±3	9.00	-0.016 ±0.005	-0.034 ±0.013	-0.036 ±0.006		
ALV522-1-1(2)				4.91	0.513103 ±3	9.07	0.006 ±0.005	-0.010 ±0.013	-0.013 ±0.006		
ALV522-2-2	glass	FAMOUS	9.55	5.75	0.513104 ±3	9.09	0.002 ±0.004	-0.021 ±0.010	-0.017 ±0.005		
ALV523-2	glass	FAMOUS	7.90	12.50	0.513065 ±3	8.32	-0.012 ±0.005	-0.060 ±0.012	-0.031 ±0.006		
ALV523-3	glass	FAMOUS	8.29	12.07	0.513112 ±3	9.24	0.001 ±0.005	-0.015 ±0.012	-0.018 ±0.006		
ALV525-5-1	glass	FAMOUS	9.80	5.97	0.513090 ±3	8.82	0.007 ±0.005	-0.022 ±0.012	-0.012 ±0.006		
ALV525-5-3	glass	FAMOUS	9.78	5.45	0.513089 ±3	8.79	-0.013 ±0.006	-0.020 ±0.014	-0.032 ±0.006		
ALV527-1-1	glass	FAMOUS	9.65	3.84	0.513102 ±2	9.05	0.003 ±0.004	-0.035 ±0.011	-0.016 ±0.005		
ALV529-3-2	glass	FAMOUS	9.14	6.82	0.513114 ±3	9.28	-0.003 ±0.005	-0.034 ±0.012	-0.022 ±0.006		

Sample	Type	Location	MgO (wt %)	Nd (ppm)	$^{143}Nd/^{144}Nd$	$\varepsilon^{143}Nd$	$\delta^{146/144}Nd$	$\delta^{148/144}Nd$	$\delta^{146/144}Nd_{NORM}$	2 s.d.	*n*
ALV534-2-1	glass	FAMOUS	9.69	5.75	0.513086 ±4	8.74	-0.022 ±0.006	-0.030 ±0.015	-0.041 ±0.007		
EW93-09 15D	glass		7.91	10.75	0.513031 ±2	7.66	0.000 ±0.004	-0.033 ±0.009	-0.020 ±0.005		
								Average-Atlantic	**−0.024 ±0.004**	**±0.015**	*14*
Indian Ocean											
MD34 D6$	glass	SWIR	6.66	15.28	0.513043 ±2	7.89	-0.008 ±0.004	-0.023±0.009	-0.027 ±0.005		
MD37 03-01 D1-26$	glass	SEIR	8.03	7.98	0.513038 ±3	7.81	-0.004 ±0.005	-0.062 ±0.012	-0.023 ±0.006		
MD57 D9-1$	glass	CIR	8.71	3.77	0.513140 ±3	9.80	-0.008 ±0.006	-0.024 ±0.014	-0.027 ±0.006		
MD57 D9-6$	glass			4.64	0.513147 ±3	9.93	-0.009 ±0.004	-0.051 ±0.010	-0.028 ±0.005		
MD57 D'10-1$	glass		6.84	12.58	0.513058 ±3	8.20	-0.010 ±0.006	-0.036 ±0.014	-0.029 ±0.007		
MD57D13-7$	glass	CIR	7.12	12.18	0.513070 ±3	8.42	-0.004 ±0.005	-0.024 ±0.013	-0.023 ±0.006		
MD57D13-7*$				12.18	0.513075 ±3	8.53	0.004 ±0.005	-0.037 ±0.012	-0.015 ±0.006		
								Average-Indian	**−0.026 ±0.004**	**±0.008**	*6*
Pacific Ocean											
CYP78 04-06	glass		7.84	9.72	0.5131411 ±2	9.81	-0.006 ±0.005	-0.066 ±0.011	-0.025 ±0.005		
CYP78 12-35	glass		7.81	9.22	0.513151 ±3	10.00	-0.017 ±0.005	-0.056 ±0.012	-0.036 ±0.006		
CYP78 18-65	glass		7.75	10.04	0.513148 ±3	9.95	-0.013 ±0.005	-0.055 ±0.012	-0.032 ±0.006		
GN4-1$	glass	Garrett FZ	8.05	3.49	0.513272 ±3	12.36	-0.019 ±0.005	-0.021 ±0.011	-0.022 ±0.005		
GN4-1(2)				5.50	0.513267 ±4	12.26	-0.025 ±0.007	-0.081 ±0.016	-0.045 ±0.007		

Sample	Type	Location	MgO (wt %)	Nd (ppm)	$^{143}Nd/^{144}Nd$	$\varepsilon^{143}Nd$	$\delta^{146/144}Nd$	$\delta^{148/144}Nd$	$\delta^{146/144}Nd_{NORM}$	2 s.d.	*n*
GN4-11$	glass	Garrett FZ	8.95	4.10	0.513263 ±2	12.19	-0.029 ±0.004	-0.055 ±0.011	-0.033 ±0.005		
GN4-11(2)				5.52	0.513259 ±3	12.11	-0.010 ±0.005	-0.057 ±0.012	-0.029 ±0.006		
GN12-10	glass	Garrett FZ		8.80	0.513273 ±3	12.38	0.003 ±0.005	-0.046 ±0.011	-0.016 ±0.006		
GN13-1$	glass	Garrett FZ	8.79	4.47	0.513300 ±3	12.91	-0.006 ±0.005		-0.009 ±0.005		
GN13-1(2)				5.74	0.513292 ±3	12.75	-0.014 ±0.006	-0.039 ±0.014	-0.034 ±0.007		
GN13-6	glass	Garrett FZ	7.57	10.70	0.513218 ±3	11.32	0.005 ±0.005	-0.030 ±0.013	-0.014 ±0.006		
GN13-8$	glass	Garrett FZ	6.87	9.21	0.513218 ±3	11.31	-0.019 ±0.005	-0.044 ±0.012	-0.023 ±0.005		
GN13-8(2)				12.19	0.513214 ±2	11.23	-0.004 ±0.004	-0.051 ±0.010	-0.023 ±0.005		
Searise2 DR2-2	glass		6.66	10.04	0.513193 ±3	10.82	-0.005 ±0.004	-0.035 ±0.011	-0.024 ±0.005		
SO12 143-1	glass		7.68	10.77	0.513044 ±2	7.91	-0.004 ±0.004	-0.037 ±0.009	-0.023 ±0.005		
SO22 29D58a	glass		7.76	10.14	0.513114 ±2	9.28	-0.012 ±0.004	-0.024 ±0.010	-0.031 ±0.005		
Venture VE32	glass		7.31	13.41	0.513041 ±2	7.86	-0.001 ±0.005	-0.044 ±0.011	-0.020 ±0.005		
								Average-Pacific	**−0.025 ±0.004**	**±0.014**	*13*
								Average-MORB	**−0.025 ±0.002**	**±0.013**	*33*
Ocean Island											
BIR-1$	whole rock	Iceland	9.69	2.33	0.513088 ±19	8.78			0.013	±0.015	*9*
BHVO-1$	whole rock	Hawaii	7.21	24.78	0.512982 ±9	6.72			-0.031	±0.014	*11*
BHVO-2$	whole rock	Hawaii	7.26	24.39	0.512982 ±19	6.71			-0.030	±0.014	*17*

Sample	Type	Location	MgO (wt %)	Nd (ppm)	$^{143}Nd/^{144}Nd$	$\varepsilon^{143}Nd$	$\delta^{146/144}Nd$	$\delta^{148/144}Nd$	$\delta^{146/144}Nd_{NORM}$	2 s.d.	*n*
PNDR 3-4	glass	Pitcairn	2.26	81.66	0.512478 ±3	-3.12	-0.006 ±0.004	-0.068 ±0.011	-0.026 ±0.005		
PNDR 3-8	glass	Pitcairn	2.22	42.75	0.512545 ±3	-1.82	-0.023 ±0.005	-0.103 ±0.013	-0.042 ±0.006		
PNDR 3-10	glass	Pitcairn	2.22	23.99	0.512633 ±2	-0.10	-0.017 ±0.004	-0.057 ±0.011	-0.036 ±0.005		
PNDR 8-7	glass	Pitcairn	2.68	83.00	0.512443 ±3	-3.80	0.007 ±0.005	-0.025 ±0.012	-0.013 ±0.006		
PNDR 12-3	glass	Pitcairn	1.33	76.06	0.512456 ±2	-3.56	-0.036 ±0.005	-0.108 ±0.012	-0.055 ±0.006		
PNDR 14-6	glass	Pitcairn	5.39	29.12	0.512640 ±3	0.03	-0.003 ±0.005	-0.045 ±0.013	-0.022 ±0.006		
PNDR 14-7	glass	Pitcairn	5.59	27.35	0.512635 ±3	-0.06	-0.021 ±0.005	-0.056 ±0.011	-0.040 ±0.005		
RRT C29	glass	Rurutu	10.70	41.00	0.512902 ±3	5.14	-0.021 ±0.005	-0.076 ±0.012	-0.040 ±0.006		
RRT C65	glass	Rurutu	14.66	34.30	0.512877 ±3	4.67	-0.042 ±0.005	-0.092 ±0.012	-0.061 ±0.006		
MGA C23	glass	Mangaia	7.91	14.83	0.512869 ±3	4.51	-0.011 ±0.005	-0.045 ±0.011	-0.030 ±0.006		
SM 33	whole rock	Sao Miguel	11.32	49.25	0.512763 ±3	2.44	-0.018 ±0.006	-0.058 ±0.014	-0.037 ±0.007		
SM 33*				47.81	0.512774 ±2	2.66	-0.005 ±0.004	-0.053 ±0.011	-0.024 ±0.005		
								Average-OIB^	**−0.035 ±0.008**	**±0.026**	*13*
Other (Continental) Intraplate											
BCR-1$	whole rock	Columbia River	3.47	28.67	0.512632 ±5	-0.10			-0.031	±0.015	*5*
BCR-2$	whole rock	Columbia River	3.60	28.29	0.512633 ±6	-0.08			-0.023	±0.015	*2*
B-EN$	whole rock	France	13.06	66.41	0.512874 ±3	4.62			-0.037	±0.015	*5*
AMB-10$	whole rock	New Zealand	17.79	20.22	0.512811 ±3	3.37	-0.046 ±0.004	-0.100 ±0.011	-0.023 ±0.005		

Sample	Type	Location	MgO (wt %)	Nd (ppm)	$^{143}Nd/^{144}Nd$	$\varepsilon^{143}Nd$	$\delta^{146/144}Nd$	$\delta^{148/144}Nd$	$\delta^{146/144}Nd_{NORM}$	2 s.d.	*n*
AMB-22$	whole rock	New Zealand	18.42	21.27	0.512804 ±2	3.25	-0.047 ±0.004	-0.100 ±0.009	-0.024 ±0.005		
AMB-41$	whole rock	New Zealand	10.94	34.05	0.512788 ±3	2.93	-0.042 ±0.004	-0.092 ±0.011	-0.019 ±0.005		
AMC-9$	whole rock	New Zealand	12.05	29.99	0.512788 ±2	2.93	-0.042 ±0.004	-0.105 ±0.009	-0.019 ±0.005		
AMG-8$	whole rock	New Zealand	13.02	29.72	0.512804 ±2	3.23	-0.050 ±0.004	-0.093 ±0.009	-0.027 ±0.005		
DI-24	whole rock	Baffin Is	24.46	3.35	0.513108 ±2	9.17	-0.031 ±0.004	-0.048 ±0.010	-0.034 ±0.004		
DI-27	whole rock	Baffin Is	18.62	2.93	0.513070 ±3	8.43	-0.050 ±0.004	-0.080 ±0.011	-0.054 ±0.005		
PI-40	whole rock	Baffin Is	29.24	1.92	0.513116 ±3	9.33	-0.036 ±0.004	-0.055 ±0.010	-0.040 ±0.005		
GOR 94-01	whole rock	Gorgona	18.04	2.33	0.513186 ±3	10.70	0.005 ±0.005	0.016 ±0.013	0.001 ±0.005		
GOR 94-28	whole rock	Gorgona	25.36	1.79	0.513207 ±4	11.10	-0.006 ±0.008	0.019 ±0.019	-0.009 ±0.008		
								Average-Other	**−0.026 ±0.008**	**±0.028**	*13*
Island Arc											
116852-1	whole rock	Sulu Range	9.20	1.68	0.513016 ±6	7.38	-0.032 ±0.009	-0.120 ±0.023	-0.035 ±0.010		
116852-2	whole rock	Ulawun	4.69	3.32	0.512919 ±4	5.48	-0.015 ±0.008	-0.060 ±0.020	-0.019 ±0.008		
116852-3	whole rock	Wulai Island	5.60	4.14	0.512998 ±3	7.02	-0.035 ±0.005	-0.075 ±0.012	-0.039 ±0.005		
116852-4	whole rock	Bagum	6.90	7.25	0.513028 ±3	7.61	0.025 ±0.005	0.037 ±0.012	0.022 ±0.005		
116852-5	whole rock	Kimbe Island	10.10	3.56	0.513051 ±3	8.05	-0.020 ±0.005	-0.059 ±0.012	-0.024 ±0.005		
116852-6	whole rock	Unea Island	4.45	8.60	0.513008 ±2	7.23	-0.018 ±0.004	-0.045 ±0.010	-0.021 ±0.005		

Sample	Type	Location	MgO (wt %)	Nd (ppm)	$^{143}Nd/^{144}Nd$	$\varepsilon^{143}Nd$	$\delta^{146/144}Nd$	$\delta^{148/144}Nd$	$\delta^{146/144}Nd_{NORM}$	2 s.d.	*n*
116852-7	whole rock	Garove Island	5.30	11.12	0.513066 ±2	8.35	-0.007 ±0.004	-0.042 ±0.011	-0.011 ±0.005		
116852-8	whole rock	Garove Island	7.95	5.53	0.513049 ±3	8.01	-0.017 ±0.005	-0.057 ±0.012	-0.021 ±0.005		
116852-9	whole rock	Nundua Island	9.15	7.46	0.513103 ±5	9.07	-0.020 ±0.008	-0.079 ±0.020	-0.024 ±0.008		
116852-10	whole rock	Nundua Island	6.45	10.14	0.513027 ±2	7.58	0.006 ±0.004	-0.014 ±0.009	0.002 ±0.004		
116852-11	whole rock	Undaka Island	10.80	8.54	0.513041 ±2	7.87	-0.028 ±0.004	-0.069 ±0.011	-0.032 ±0.005		
116852-12	whole rock	Narage Island	5.80	24.90	0.513058 ±2	8.19	-0.014 ±0.004	-0.047 ±0.009	-0.017 ±0.004		
								Average-IAB	**−0.018 ±0.011**	**±0.033**	*12*
								Average-Mantle$	**−0.018 ±0.022**	**±0.053**	*8*
								Bulk Silicate Earth Average	**−0.024 ±0.003**	**±0.031**	*80*

Table 2: Model parameters for the calculation of Nd isotope fractionation during non-modal batch melting.

Phase	**Starting fraction***	**Melting reaction***	**D_{Nd}**
Olivine	0.52	0.08	0.000049
Orthopyroxene	0.18	−0.19	0.0087
Clinopyroxene	0.24	0.81	0.4076
Garnet	0.06	0.3	0.0637
		Bulk D_0	0.1032
		Bulk P	0.3476

Table 3: Parameters used in the calculation of force constants for Nd isotopes in minerals and melts.

	$C_{N\,Nd}$	S_{Nd}	$C_{N\,O}$	S_O	$r_{Nd-O}M$ (pm)	$r_{Nd-O}Cal$ (pm)	K_f^{Nd-O} (N/m)	K_T^{Nd-O} (N/m)
Melts								
Nd_2O_3	6	0.5	4	0.5	234[1]	236.3	49.6	101.5
Nd_2O_3	6	0.5	3	0.667	263[1]	234.3	46.6	95.3
Minerals								
Clinopyroxene (M2-site)	8	0.38	3.75	0.533	249.8[2]	248.9	32.6	88.9
Garnet (X-site)	8	0.38	4	0.5	242.3[3]	248.9	33.5	91.3

Research Highlights

- First comprehensive study of Nd stable isotopes in wide range of terrestrial basalts.
- Partial melting modelling demonstrates that $\delta^{146}Nd$ is unfractionated upon melting.
- Confirmation the bulk silicate Earth and chondrites have the indistinguishable $\delta^{146}Nd$.
- Variations in $\delta^{146}Nd$ induce no analytical artefacts in radiogenic isotope compositions.

Declaration of interests

☒ The authors declare that they have no known competing financial interests or personal relationships that could have appeared to influence the work reported in this paper.

Figure 1

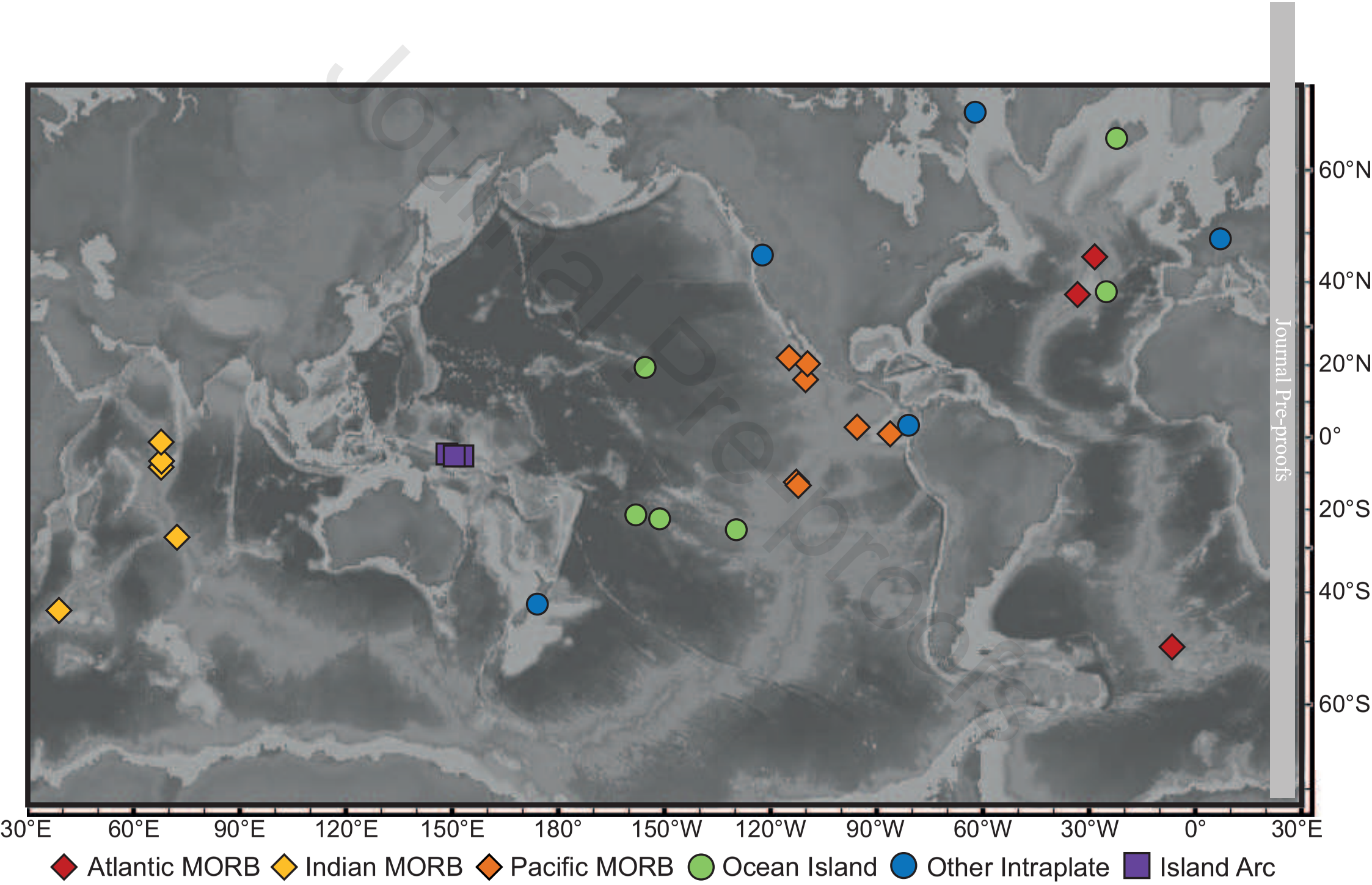

Figure 2

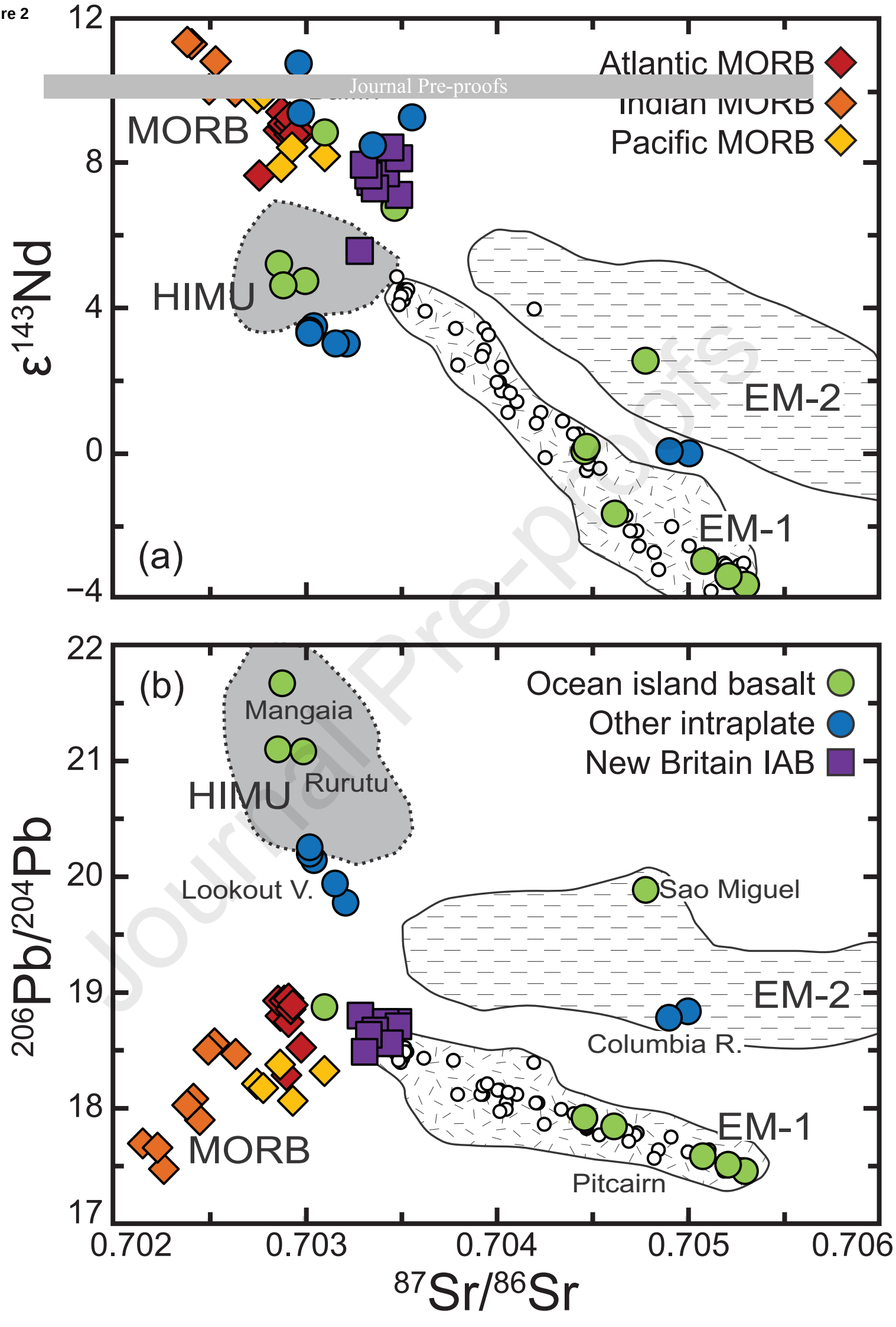

Figure 3

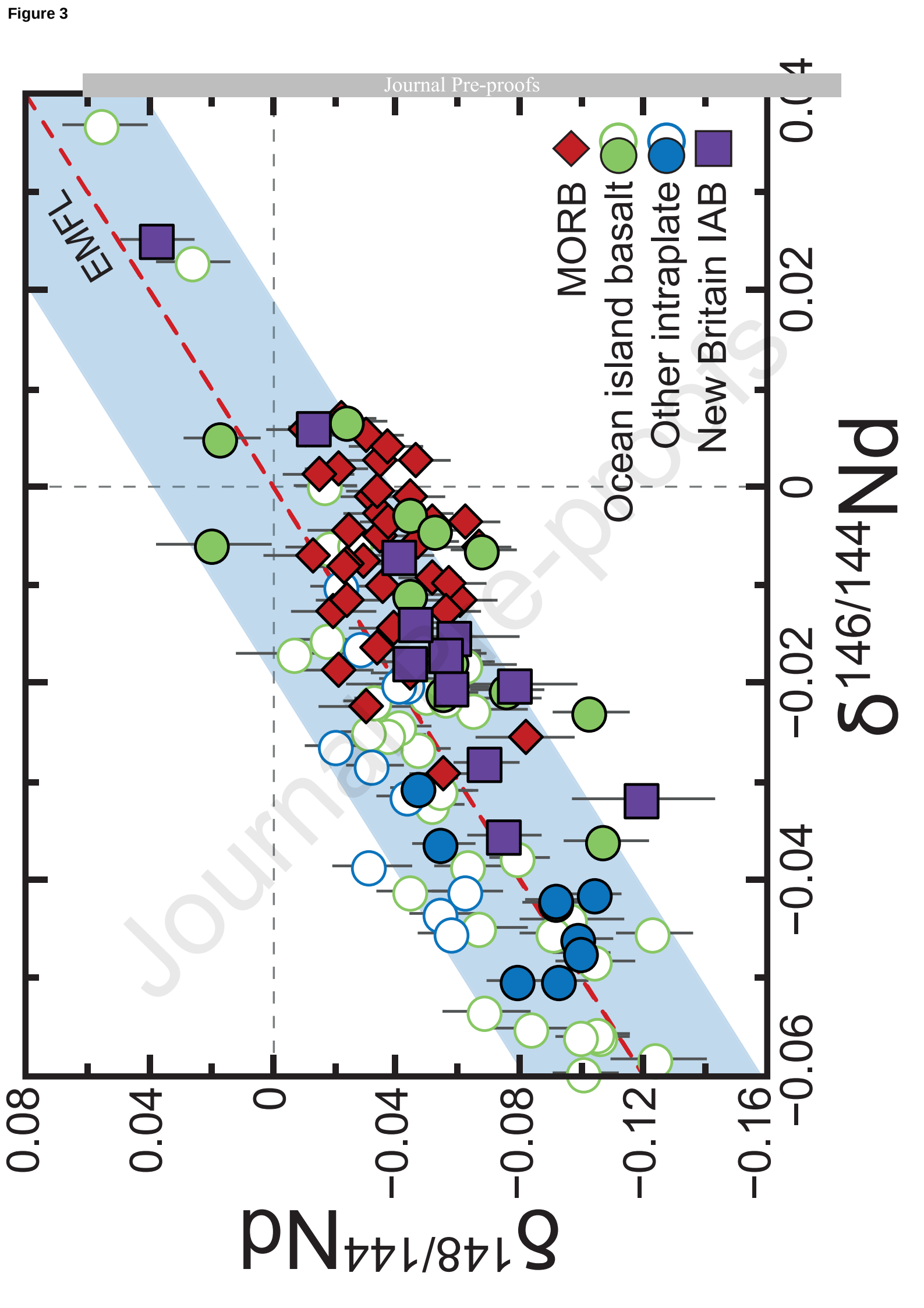
Journal Pre-proofs
EMFL
MORB
Ocean island basalt
Other intraplate
New Britain IAB
$\delta^{146/144}Nd$
$\delta^{148/144}Nd$
0.08
0.04
0
−0.04
−0.08
−0.12
−0.16
0.02
0
−0.02
−0.04
−0.06

Figure 4

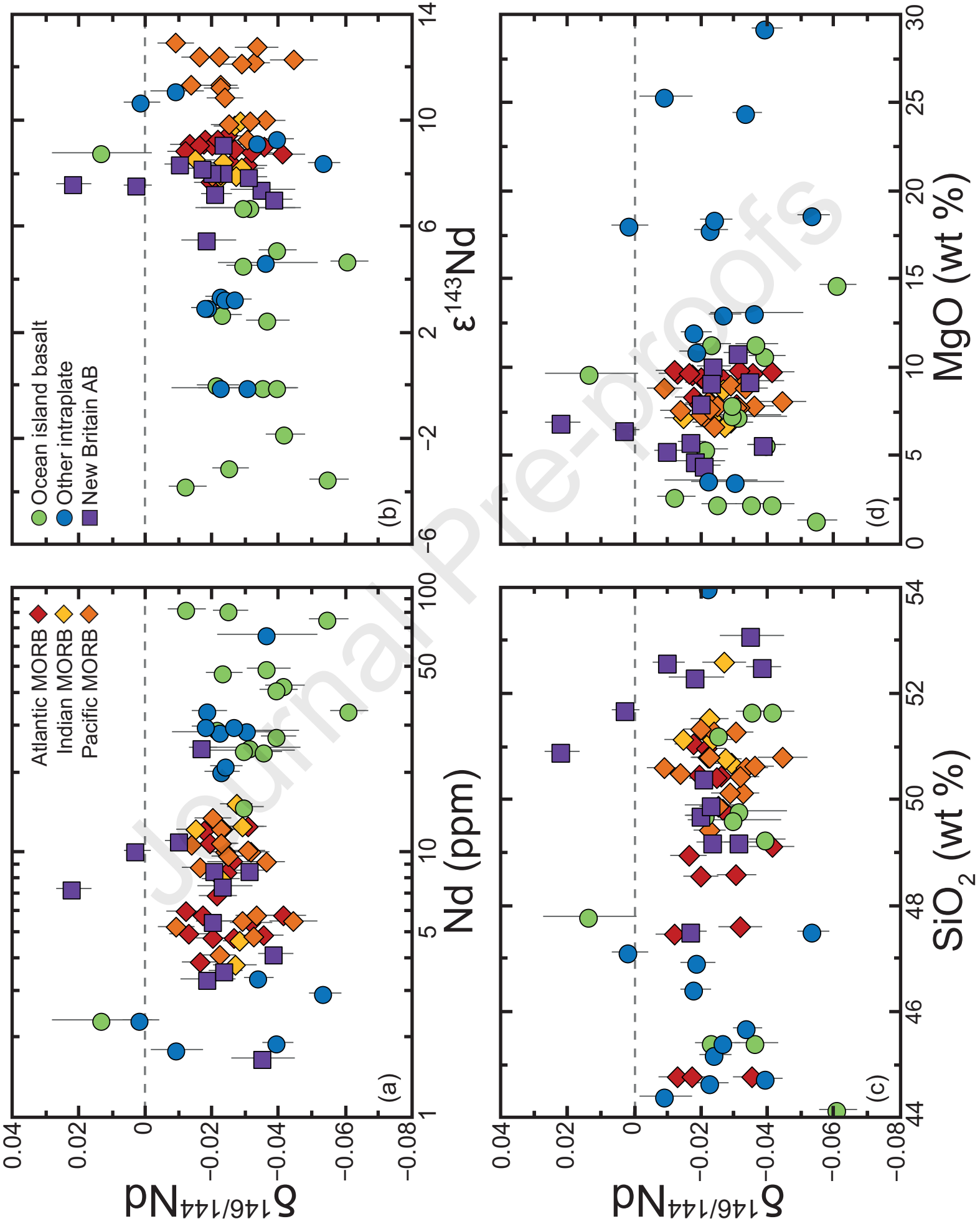

Figure 5

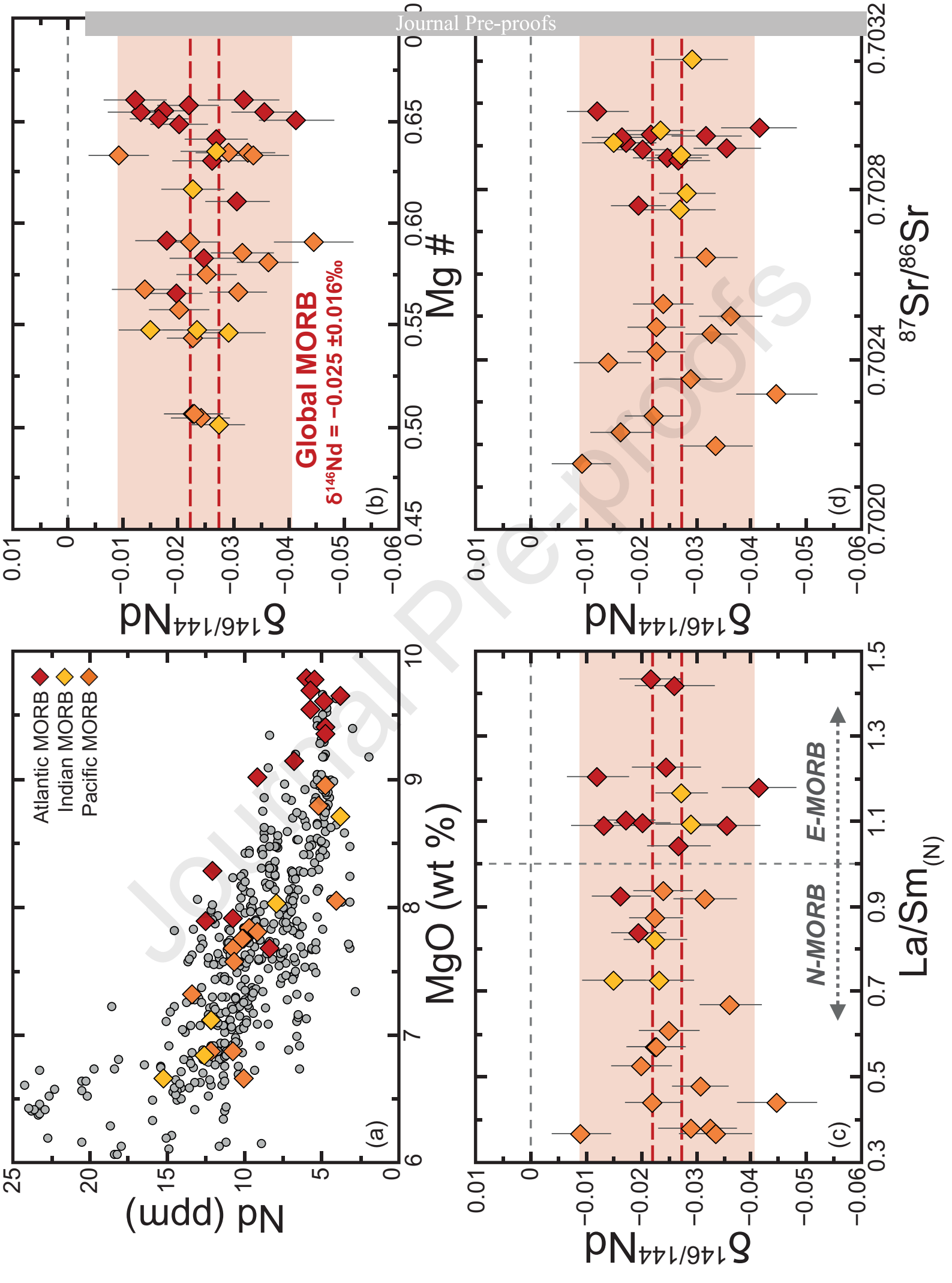

Figure 6

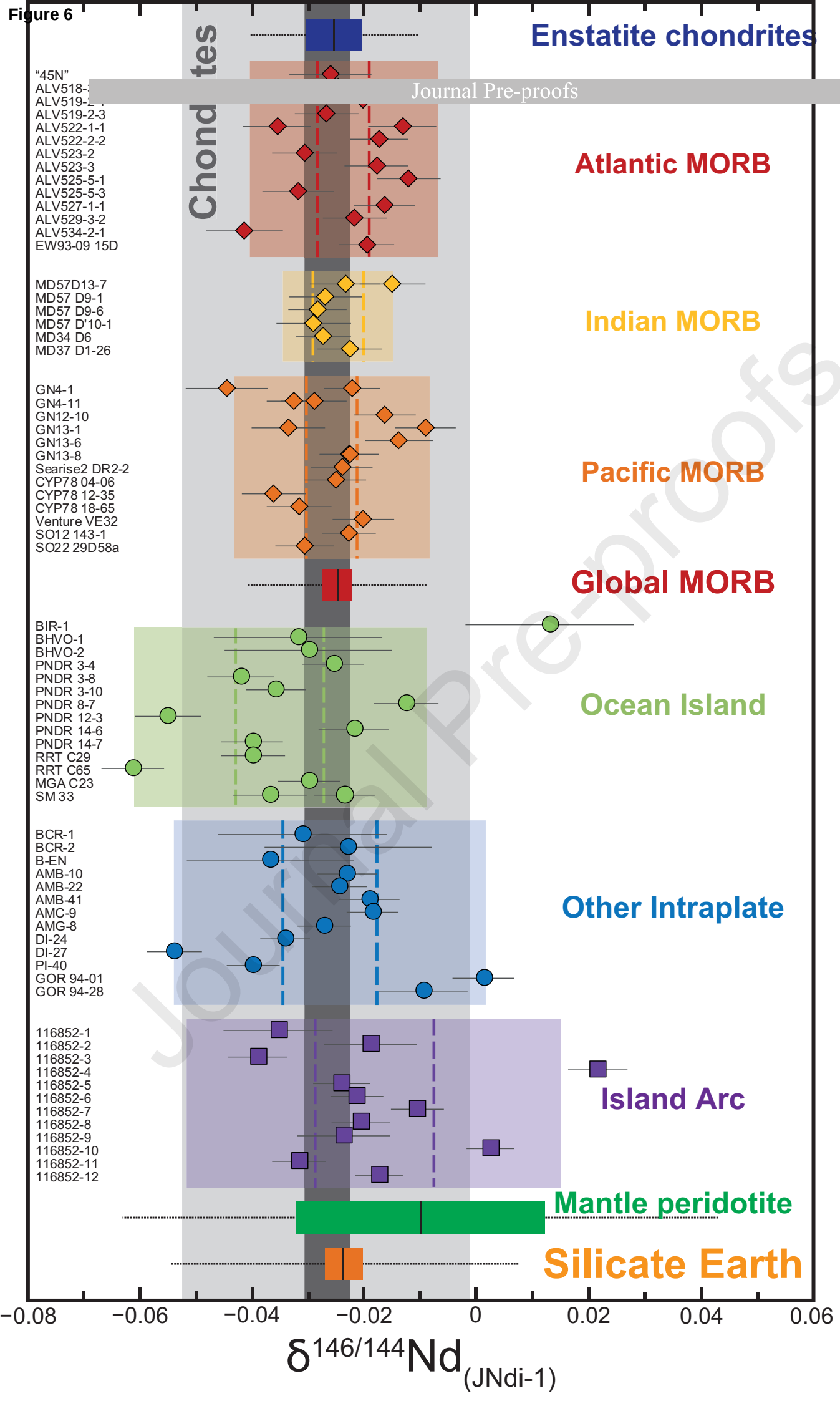

Figure 7

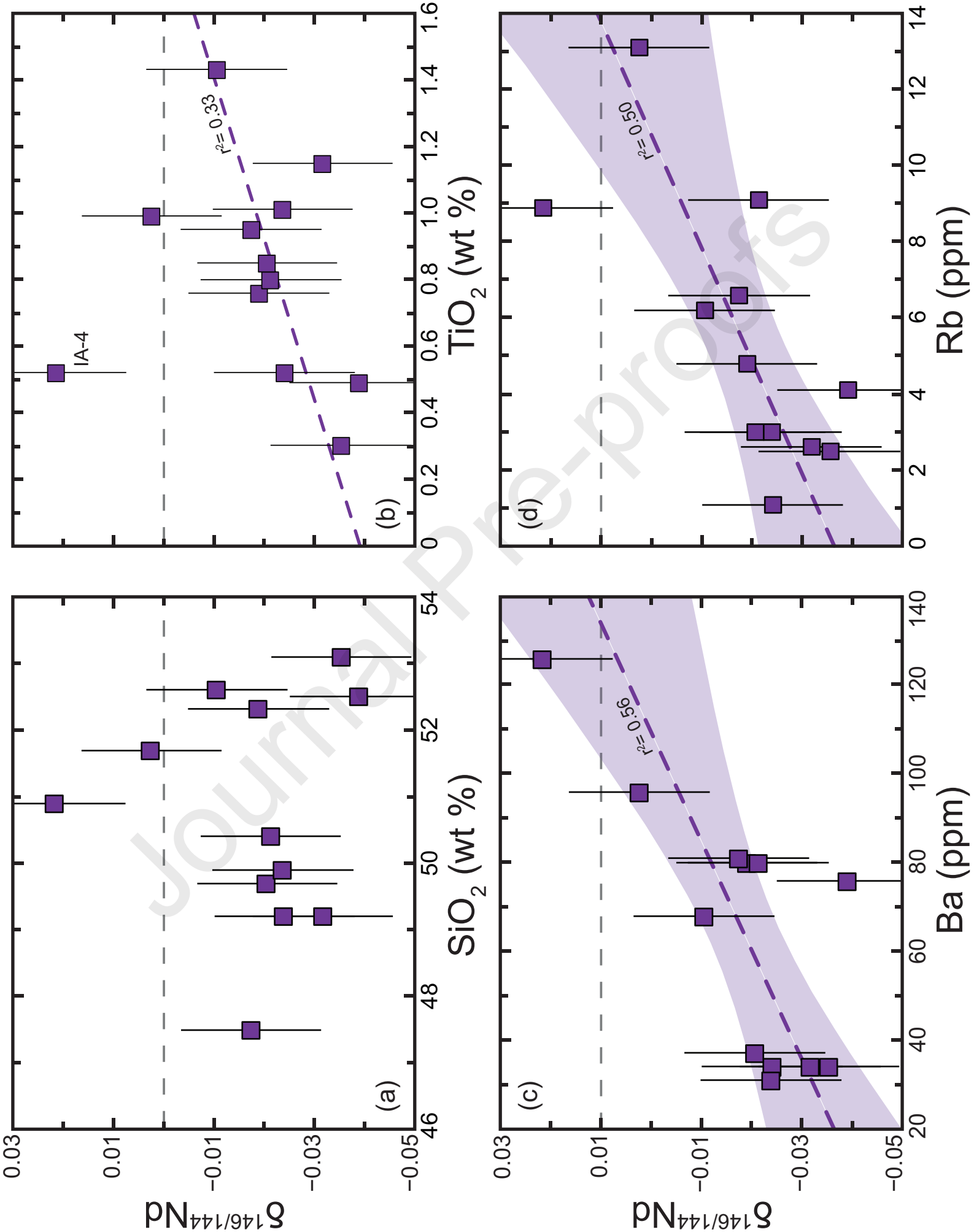

Figure 8

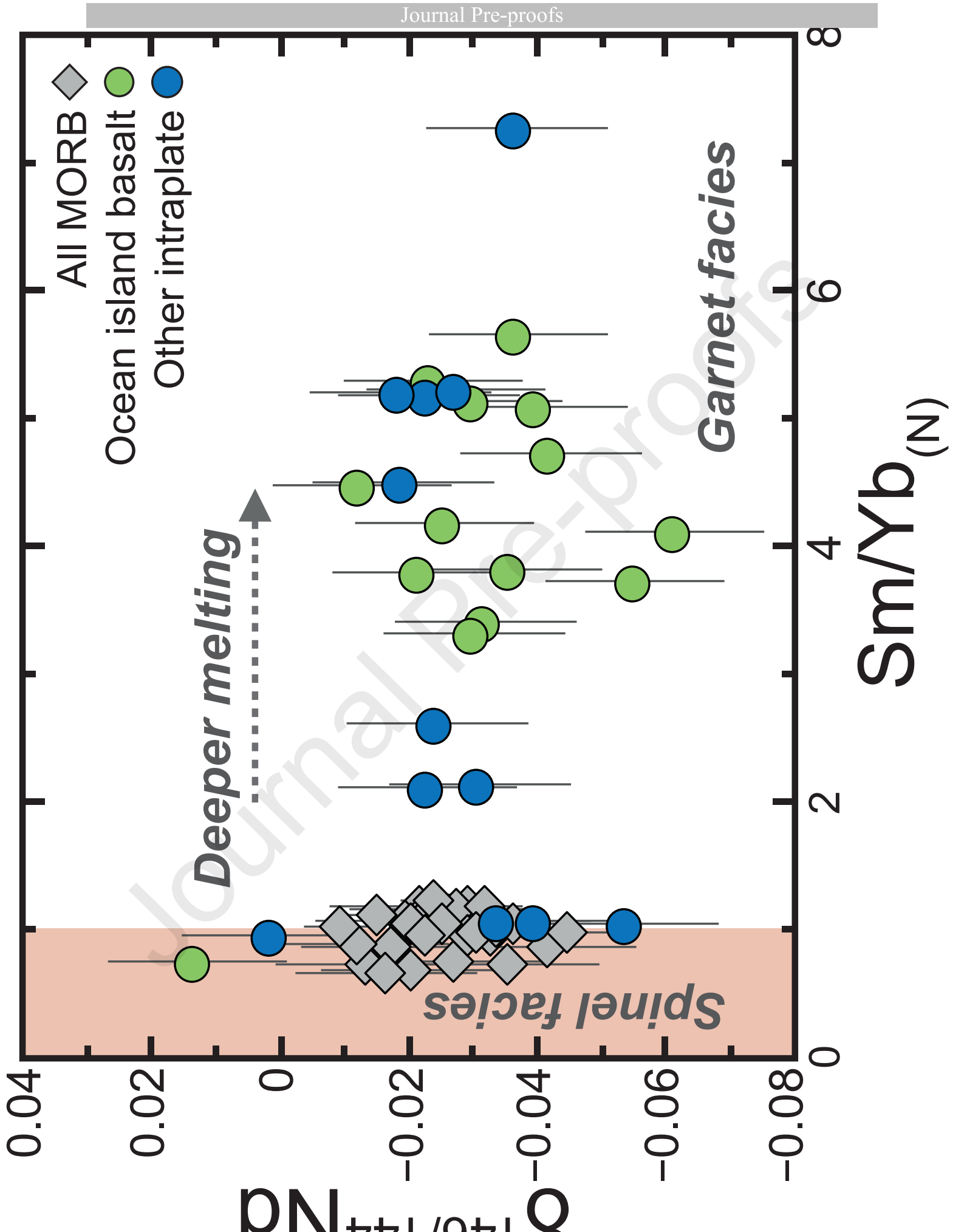
Journal Pre-proofs
All MORB
Ocean island basalt
Other intraplate
Deeper melting
Garnet facies
Spinel facies
Sm/Yb(N)
δ146/144Nd
0.04
0.02
0
−0.02
−0.04
−0.06
−0.08
0
2
4
6
8

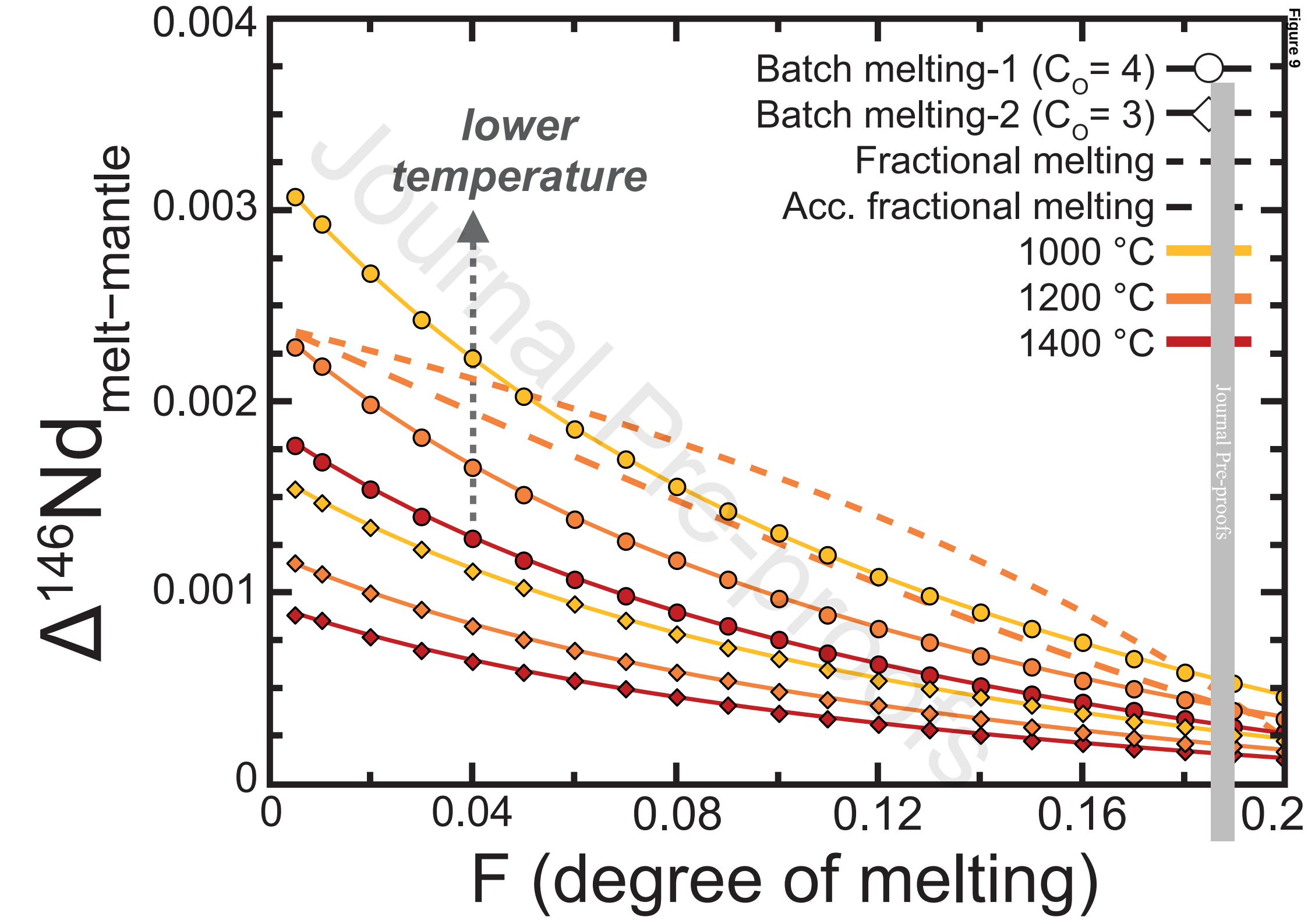
Figure 9
Batch melting-1 (C_o= 4)
Batch melting-2 (C_o= 3)
Fractional melting
Acc. fractional melting
1000 °C
1200 °C
1400 °C
lower temperature
$\Delta^{146}Nd_{melt-mantle}$
F (degree of melting)
0.004
0.003
0.002
0.001
0
0.04
0.08
0.12
0.16
0.2
Journal Pre-proofs

Figure 10

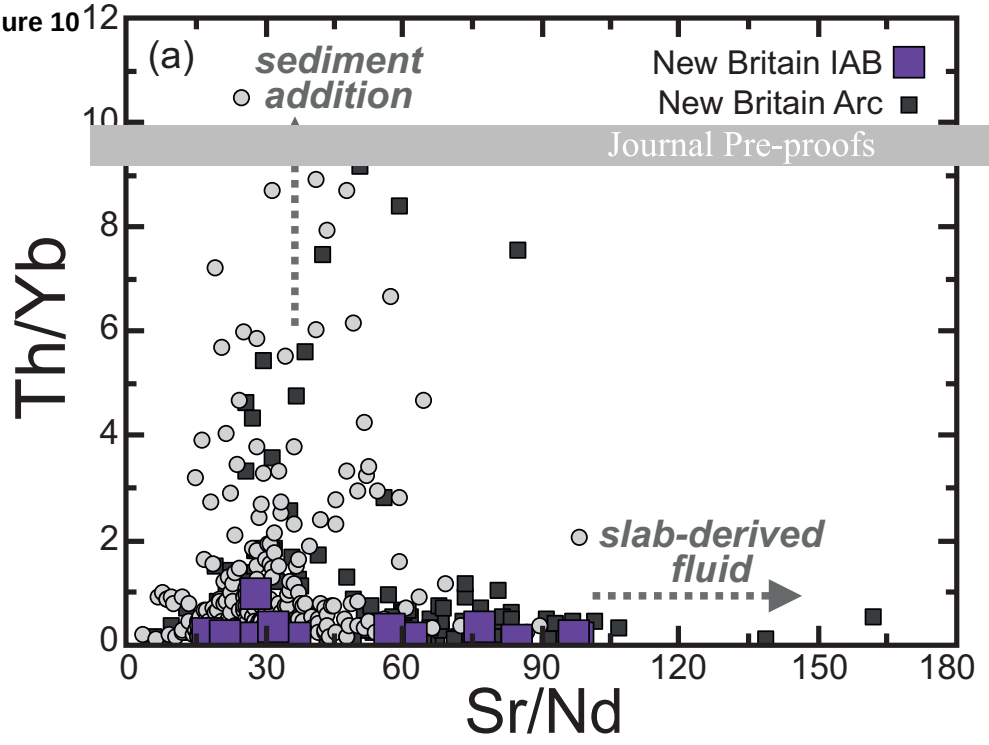

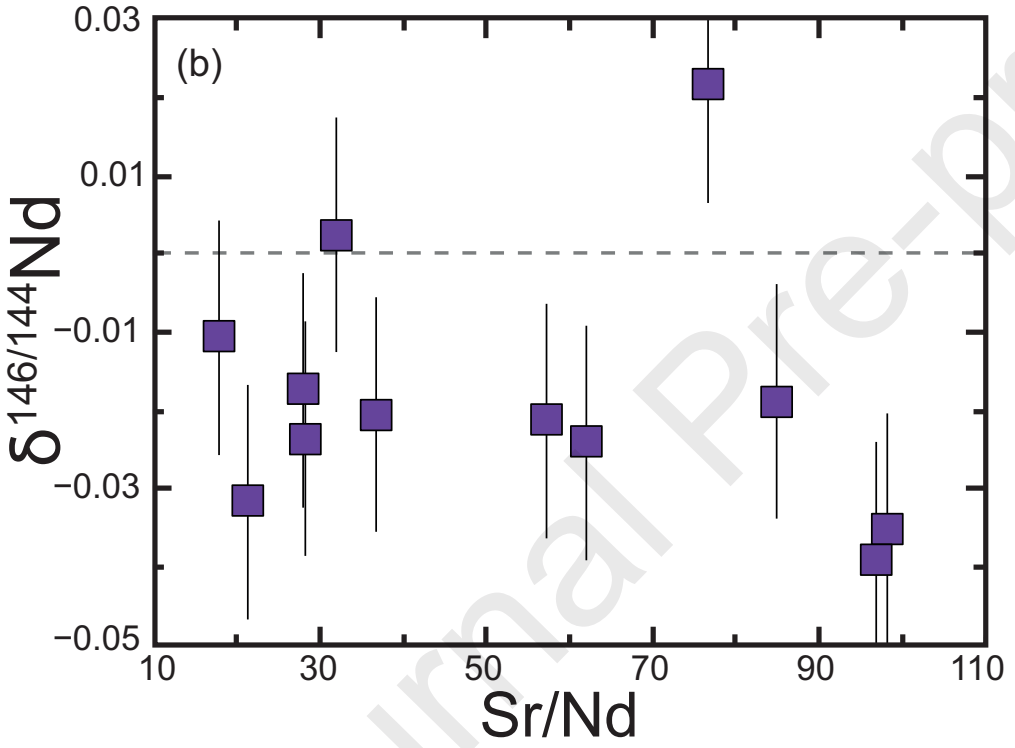

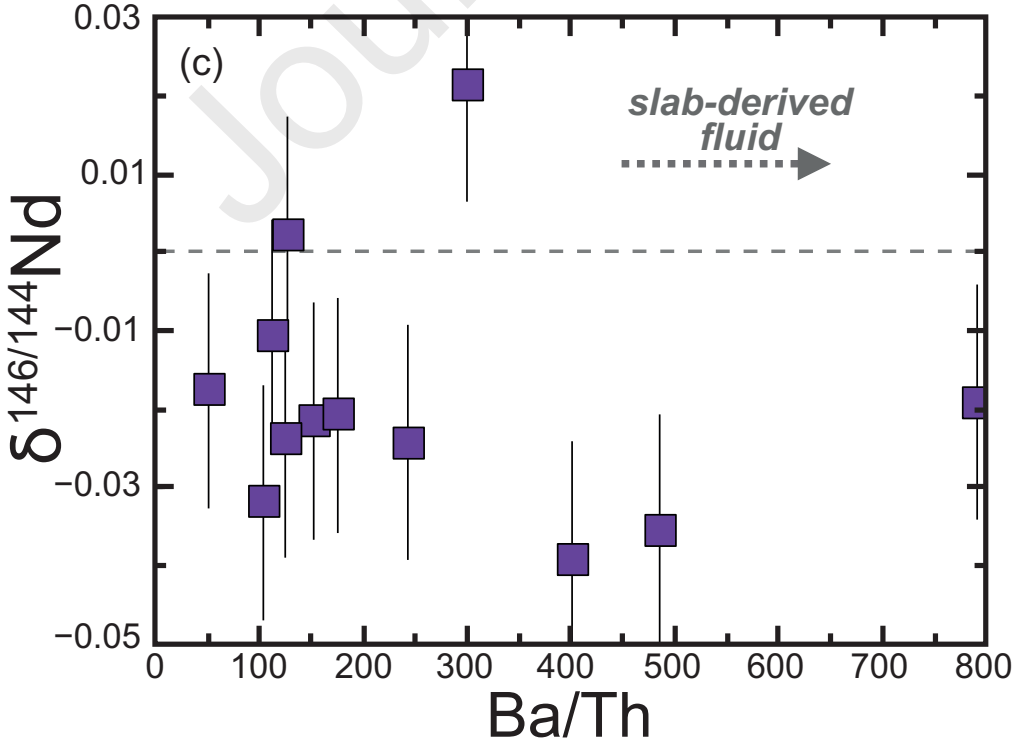

Figure 11

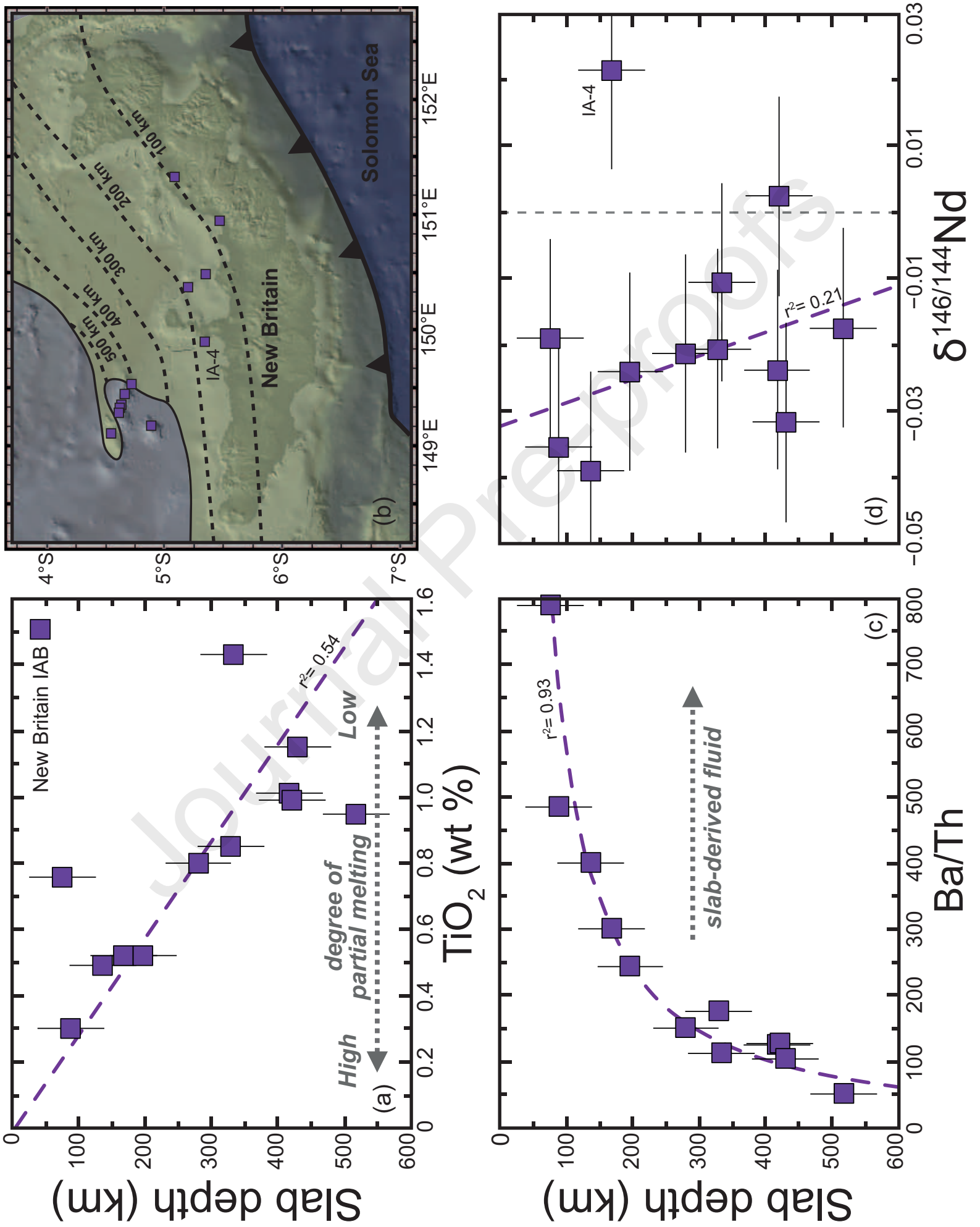

Figure 12